

1 **Wind-driven evolution of the North Pacific subpolar gyre over the last**
2 **deglaciation**

3

4 William R Gray^{1,2*}, Robert CJ Wills³, James WB Rae², Andrea Burke², Ruza F
5 Ivanovic⁴, William HG Roberts⁵, David Ferreira⁶, Paul J Valdes⁷

6 ¹Laboratoire des Sciences du Climat et de l'Environnement (LSCE/IPSL), Gif-sur-
7 Yvette, France

8 ²School of Earth and Environmental Science, University of St Andrews, UK

9 ³Department of Atmospheric Sciences, University of Washington, USA

10 ⁴School of Earth & Environment, University of Leeds, UK

11 ⁵Geography and Environmental Sciences, Northumbria University, UK

12 ⁶Department of Meteorology, University of Reading, UK

13 ⁷School of Geographical Sciences, University of Bristol, UK

14

15 *corresponding author: william.gray@lsce.ipsl.fr

16

17 *Key points*

- 18 • Planktic foraminiferal $\delta^{18}\text{O}$ data indicate that the North Pacific subpolar gyre
19 expanded southward by $\sim 3^\circ$ during the Last Glacial Maximum
- 20 • Climate models show that changes in gyre extent/strength are driven by the
21 response of the westerlies to ice sheet albedo and topography
- 22 • Proxy data and model simulations indicate that the gyre boundary and winds
23 began to migrate northward at ~ 17 -16 ka, during Heinrich Stadial 1

24

25 *Abstract*

26 North Pacific atmospheric and oceanic circulations are key missing pieces in
27 our understanding of the reorganisation of the global climate system since the Last
28 Glacial Maximum (LGM). Here, using a basin-wide compilation of planktic
29 foraminiferal $\delta^{18}\text{O}$, we show that the North Pacific subpolar gyre extended $\sim 3^\circ$ further
30 south during the LGM, consistent with sea surface temperature and productivity proxy
31 data. Analysis of an ensemble of climate models indicates that the expansion of the
32 subpolar gyre was associated with a substantial gyre strengthening. These gyre
33 circulation changes were driven by a southward shift in the mid-latitude westerlies and
34 increased wind-stress from the polar easterlies. Using single-forcing model runs, we
35 show these atmospheric circulation changes are a non-linear response to the combined
36 topographic and albedo effects of the Laurentide Ice Sheet. Our reconstruction suggests
37 the gyre boundary (and thus westerly winds) began to migrate northward at ~ 17 -16 ka,
38 during Heinrich Stadial 1.

39

40 *Plain language summary*

41 Despite the North Pacific's importance in the global climate system, changes in
42 the circulation of this region since the last ice age are poorly understood. Today, the
43 North Pacific Ocean has very different properties north and south of $\sim 40^\circ\text{N}$: to the
44 south, the warm surface waters form a circulation cell that moves clockwise (the
45 subtropical gyre); to the north, the cold surface waters form a circulation cell that moves
46 anti-clockwise (the subpolar gyre). This difference in surface ocean circulation north
47 and south of $\sim 40^\circ\text{N}$ is determined by the wind patterns. Here, using a compilation of
48 oxygen isotopes measured in the carbonate shells of fossil plankton from sediment
49 cores across the basin, which tracks changes in the spatial pattern of temperature, we
50 reconstruct how the position of the boundary between the gyres changed since the last

51 ice age. Our results show that the boundary between the gyres was shifted southward
52 by $\sim 3^\circ$ during the last ice age; this indicates that the westerly winds were also shifted
53 southward at this time. Using numerical simulations of the climate, we find that this ice
54 age shift in the westerly winds is primarily due to the presence of a large ice sheet over
55 North America.

56

57 **1. Introduction**

58 Despite the North Pacific's importance in the global climate system, the
59 reorganisation of surface ocean and atmosphere in this region during the Last Glacial
60 Maximum (LGM, ~ 20 ka) and the last deglaciation (~ 10 - 20 ka, 'the deglaciation' from
61 here on) remain poorly constrained. Changes in atmospheric and surface ocean
62 circulation within the North Pacific are potentially important drivers of observed
63 changes in the overturning circulation and biogeochemistry of the North Pacific during
64 the LGM and deglaciation, suggested to play a role in regulating atmospheric CO₂
65 (Keigwin, 1998; Okazaki *et al.*, 2010; Rae *et al.*, 2014; Gray *et al.*, 2018). The
66 overturning and gyre circulations are also important influences on poleward ocean heat
67 transport. Large changes in the hydroclimate of western North America during the
68 LGM and the deglaciation (e.g. Oviatt *et al.*, 1999; Nelson *et al.*, 2005; Lyle *et al.*,
69 2012; McGee *et al.*, 2012; Kirby *et al.*, 2013; Ibarra *et al.*, 2014) have been suggested
70 to result from the reorganisation of North Pacific atmospheric circulation (e.g. Oster *et*
71 *al.*, 2015; Wong *et al.*, 2016; Lora *et al.*, 2017; Lora, 2018), with early modelling work
72 suggesting a southward displacement of the westerly jet with the presence of the
73 Laurentide Ice Sheet (Manabe & Broccoli, 1985; Bartlein *et al.*, 1998). However,
74 evidence for this atmospheric reorganisation has not yet been identified in marine
75 records.

76

77 Driven by the opposite signs of the climatological wind stress curl ($\nabla \times \tau$), the
78 subtropical and subpolar gyres of the North Pacific Ocean have vastly different physical
79 and chemical properties (Boyer *et al.*, 2013; Key *et al.*, 2015). The boundary between
80 the gyres (defined as the point between the gyres at which the barotropic streamfunction
81 [$\Psi_{\text{barotropic}} = 0$] is determined by Sverdrup balance and occurs where $\nabla \times \tau$ integrated
82 from the eastern boundary of the basin is zero (Sverdrup, 1947; Deser *et al.*, 1999).
83 Today, the gyre boundary (which broadly determines the position of the subarctic front)
84 is nearly zonal and lies at $\sim 40^\circ\text{N}$, approximately following the local $\nabla \times \tau = 0$ line.
85 South of $\sim 40^\circ\text{N}$, anticyclonic wind stress curl in the subtropical gyre (STG) results in
86 Ekman pumping (downwelling), allowing warm, nutrient-poor, surface waters to
87 accumulate. North of $\sim 40^\circ\text{N}$, cyclonic wind stress curl in the subpolar gyre (SPG)
88 results in Ekman suction (upwelling), bringing cold, nutrient-rich, waters from the
89 oceans interior into the surface. Surface ocean chlorophyll concentrations are order of
90 magnitude higher in the SPG compared to the STG. The gyre circulation also dominates
91 ocean heat transport in the Pacific (Forget and Ferreira, 2019). The relative extent and
92 the strength of the gyres therefore exerts a large influence over basin-wide ecology,
93 biogeochemistry, and climate.

94

95 Coupled climate models predict a $\sim 60\%$ increase in wind stress curl within the
96 subpolar North Pacific under glacial forcings compared to pre-industrial forcings (Gray
97 *et al.*, 2018). By Sverdrup balance (Sverdrup, 1947), this should result in a large and
98 predictable response in gyre circulation. Despite some early work suggesting the
99 subarctic front may have shifted southward during glacial times (Thompson and
100 Shackleton, 1980; Sawada and Handa, 1998), little is known about gyre circulation over

101 the deglaciation. Here, we use meridional profiles of planktic foraminiferal $\delta^{18}\text{O}$ to
102 reconstruct the position of the gyre boundary over the deglaciation. Given the relatively
103 simple dynamical link between gyre circulation and wind stress, our gyre boundary
104 reconstruction also helps constrain the deglacial reorganisation of the atmospheric
105 circulation. We use an ensemble of climate models forced by a range of boundary
106 conditions to further explore the causes and implications of our gyre boundary
107 reconstruction for the atmospheric and near-surface ocean circulations within the North
108 Pacific.

109

110 **2. Methods**

111 *2.1 $\delta^{18}\text{O}$ as a tracer of gyre circulation*

112 The large (~ 20 °C) sea surface temperature (SST) difference between the gyres
113 (Boyer *et al.*, 2013) allows us to use meridional profiles of $\delta^{18}\text{O}$ in planktic
114 foraminiferal calcite ($\delta^{18}\text{O}_{\text{calcite}}$) to trace the gyre boundary (supporting information).
115 This temperature difference between the gyres drives a calcite-water fractionation
116 ($\delta^{18}\text{O}_{\text{calcite-water}}$) that is ~ 6 ‰ greater in the SPG than the STG (Figure 1d). Therefore,
117 although the $\delta^{18}\text{O}$ of seawater ($\delta^{18}\text{O}_{\text{water}}$) is ~ 1 ‰ lighter in the SPG compared to the
118 STG due to its lower salinity (~ 1.5 PSU; Figure 1c), $\delta^{18}\text{O}_{\text{calcite}}$ is ~ 5 ‰ higher in the
119 SPG than the STG (Figure 1e). The two gyres are thus clearly delineated in the $\delta^{18}\text{O}$ of
120 planktic foraminiferal calcite predicted using modern temperature and $\delta^{18}\text{O}_{\text{water}}$ (Figure
121 1e), with the steepest meridional gradient in $\delta^{18}\text{O}_{\text{calcite}}$ at the gyre boundary (Figure 1f).
122 While there are likely to be local changes in $\delta^{18}\text{O}_{\text{water}}$ across the basin over the
123 deglaciation, a salinity difference of ~ 15 PSU would be required to equal the
124 temperature signal between the gyres. As no mechanism exists to drive such a
125 salinity/ $\delta^{18}\text{O}_{\text{water}}$ difference, temperature will always dominate the meridional $\delta^{18}\text{O}_{\text{calcite}}$

126 gradient (Figure 1f). We can therefore use meridional profiles of $\delta^{18}\text{O}_{\text{calcite}}$ to track the
127 position of the gyre boundary.

128

129 We compiled previously published planktic foraminiferal $\delta^{18}\text{O}_{\text{calcite}}$ records
130 spanning the last deglaciation from the North Pacific Ocean (Figure 1; supporting
131 information). The gyre boundary is clearly defined by the steepest meridional gradient
132 ($\Delta\delta^{18}\text{O}_{\text{calcite}}/\Delta\text{Latitude}$) in the Holocene planktic foraminiferal $\delta^{18}\text{O}_{\text{calcite}}$ data (Figure 2;
133 supporting information). The difference in meridional temperature gradient between
134 the east and west of the basin is also evident in the Holocene $\delta^{18}\text{O}_{\text{calcite}}$ data (Figure 2b).

135

136 To reconstruct position the of gyre boundary over the deglaciation, we first
137 model the $\delta^{18}\text{O}_{\text{calcite}}$ data as a function of latitude, using a general additive model
138 (GAM) in the *mgcv* package in R (Wood, 2011; Wood *et al.*, 2016) at 500 yr timesteps
139 from 18.5 to 10.5 ka (supporting information; Figures S2-4). The smoothing term was
140 calculated using generalised cross validation (GCV), and corroborated using Reduced
141 Maximum Likelihood (REML), with both methods resulting in near-identical
142 smoothing terms and model fits. We then calculate the change in gyre boundary
143 position over the deglaciation as the latitudinal shift (x°) that minimises the Euclidian
144 distance (L^2) between the Holocene (taken as 10.5 ± 0.5 ka) $\delta^{18}\text{O}_{\text{calcite}}(\text{Lat})$ GAM fit and
145 the GAM fit at each time step, computed within a 5° latitudinal band around the
146 maximum meridional $\delta^{18}\text{O}_{\text{calcite}}$ gradient in the Holocene data (supporting information;
147 Figure S5). The width of this latitudinal band has a negligible effect on our results
148 (Figure S6).

149

150 We account for the effect of whole ocean changes in sea level ($\delta^{18}\text{O}_{\text{water}}$) and
151 SST on $\delta^{18}\text{O}_{\text{calcite}}$ by subtracting the 1‰ whole ocean change in $\delta^{18}\text{O}_{\text{water}}$ (Schrag *et al.*,
152 2002) and the $\sim 2^\circ\text{C}$ global-mean change in SST from the PMIP3 climate model
153 ensemble (see below), scaling the subtracted anomalies through time in proportion to
154 the sea level curve of Lambeck *et al.* (2014). This scaling is most robust for $\delta^{18}\text{O}_{\text{water}}$
155 due to its direct correlation with global terrestrial ice volume, however the correction
156 for global SST has very little effect and is not therefore a significant source of error.
157 We opt to make this global-mean SST correction in order to minimise differences in
158 $\delta^{18}\text{O}_{\text{calcite}}$ at different time steps relating to whole-ocean SST changes (i.e. from
159 radiative forcing), rather than local SST anomalies. The calculated changes in gyre
160 boundary position (ΔLat) are given in table S2; the reported uncertainty in ΔLat is
161 derived by quadratically propagating the uncertainty in the $\delta^{18}\text{O}_{\text{calcite}}(\text{Lat})$ GAM fits,
162 and is typically $\pm 0.9^\circ$ (1σ).

163

164 2.2 General circulation models

165 We analysed an ensemble of general circulation models forced with pre-
166 industrial and glacial boundary conditions from the Coupled Model Intercomparison
167 Project phase 5 (CMIP5, Taylor *et al.* 2012) and the Paleoclimate Model
168 Intercomparison Project phase 3 (PMIP3, Braconnot *et al.* 2012). We include all four
169 models for which both wind stress and barotropic stream function are available
170 (supporting information). We also analyse results from a single model (HadCM3)
171 where LGM greenhouse gases, ice sheet topography (‘green mountains’), and ice sheet
172 albedo (‘white plains’) forcing were changed individually (Roberts and Valdes, 2017),
173 as well as a series of HadCM3 runs where all forcings and boundary conditions are
174 changed progressively over the deglaciation in 500 yr ‘snapshots’ (as used by Morris

175 *et al.*, 2018), broadly following the PMIP4 protocol (Figure S8; see Ivanovic *et al.*,
176 2016 and supporting information).

177

178 **3. Results and Discussion**

179 *3.1 LGM planktic foraminiferal $\delta^{18}O$, SST, and productivity*

180 While sites that today are located well within either the modern SPG or STG
181 display an LGM difference in $\delta^{18}O_{\text{calcite}}$ of $\sim 1\text{-}1.5\text{‰}$, sites located within the transition
182 zone between the gyres display a much greater change of up to $\sim 3\text{‰}$ (Figure 1). This
183 anomalously large glacial increase in $\delta^{18}O_{\text{calcite}}$ is observed in transition zone sites in
184 the east and west of the basin. The Holocene $\delta^{18}O_{\text{calcite}}$ of sites located in today's
185 transition zone typically falls about half-way between the $\delta^{18}O_{\text{calcite}}$ of the SPG and
186 STG. In contrast, during the LGM the $\delta^{18}O_{\text{calcite}}$ of these same sites is almost identical
187 to the $\delta^{18}O_{\text{calcite}}$ of sites located well within the SPG. This pattern is indicative of a
188 southward shift in the boundary between the SPG and STG, such that sites that are
189 located within the transition zone today were located in (or felt a much greater influence
190 of) the SPG during the LGM.

191

192 Analysing all data from across the basin together indicates the gyre boundary
193 was positioned $3.1 \pm 0.9^\circ$ (1σ) further south during the LGM compared with its position
194 in the Holocene (Figure 2a). Analysing the data from east and west of 180° separately
195 results in a smaller change in the west of $2.0 \pm 0.9^\circ$, and a greater change in the east of
196 $6.0 \pm 1.1^\circ$ (Figure 2b). To assess if the larger change in the east of the basin may be an
197 artefact of changes in coastal upwelling, a process which could also influence the local
198 SST (and thus $\delta^{18}O_{\text{calcite}}$) anomaly, we compare the PMIP3 ensemble mean SST near
199 the eastern boundary of the basin to the zonal mean, and zonal mean east of 180° (Figure

200 S9). This analysis demonstrates no anomalous cooling at the eastern margin of the basin
201 relative to the zonal average and zonal average east of 180° in the models, suggesting
202 that coastal upwelling is unlikely to have a significant effect on our reconstruction. It
203 is more difficult to track the position of the gyre boundary in the east because of the
204 gentler slope of the meridional temperature gradient and fewer number of sites.
205 However, Sverdrup balance implies that the gyre boundary in the west of the basin
206 should respond to the integrated wind stress curl across the entire basin. Therefore, the
207 observation of a southward shift in the basin-wide gyre boundary observed in the west
208 holds regardless of how we interpret changes in the east of the basin.

209

210 Compiling all available Mg/Ca and $U^{k_{37}}$ SST data (supporting information)
211 reveals a very similar pattern of temperature changes to the foraminiferal $\delta^{18}O$ data
212 (Figure 2c). At the LGM, the SPG shows a slight warming or no change and the STG
213 shows a slight cooling, while transition zone sites on both the east and west of the basin
214 show an anomalously large cooling, supporting the southward extension of cold
215 subpolar waters during glacial times.

216

217 Analysing the North Pacific %Opal compilation of Kohfeld and Chase (2011)
218 over the last deglaciation reveals that, while the SPG and STG show a decrease in
219 %Opal during the LGM, sites in the transition zone show a ~25% increase in %Opal
220 on both sides of the basin (Figure 2d). This pattern is consistent with nutrient-rich
221 subpolar waters moving further south during the LGM and increasing local
222 productivity. The southward extension of the SPG provides a solution to the long-
223 standing question of why, while productivity decreased throughout the SPG during
224 LGM, it increased in the modern day location of the transition zone between the gyres

225 (Kienast *et al.*, 2004), leading to an anti-phased pattern of productivity between the
226 SPG and transition zone over glacial-interglacial cycles (Figure S10).

227

228 3.2 LGM General Circulation Model Simulations

229 Every model within the PMIP3 ensemble analysed exhibits a southward shift of
230 the gyre boundary under glacial forcings relative to pre-industrial, with an ensemble
231 mean change of 2.7° in the zonal-mean position of $\Psi_{\text{barotropic}} = 0$ (Figures 3 and 4), in
232 excellent agreement with our reconstruction. Consistent with the proxy data, most
233 models show a greater shift in the east of the basin, with a model mean southward shift
234 of 3.4° , and a smaller change in the west of 2.3° (Fig. 4c). In the models this southward
235 shift in the southern boundary of the SPG is caused by an overall expansion of the gyre;
236 there is no change in the location of the northern edge of the gyre, which remains at the
237 northern boundary of the basin. In addition to the expansion of the gyre, the models
238 show a substantial increase in gyre strength, with an ensemble mean $\Psi_{\text{barotropic}}$ increase
239 of 8.2 Sv (maximum north of 40°). The expansion and strengthening of the subpolar
240 gyre circulation appear tightly coupled across all models and forcings (Figure 4). This
241 coupling of the expansion and strengthening of the gyre arises as both processes are
242 driven by changes in wind stress curl, rather than through a mechanistic link based on
243 gyre dynamics.

244

245 The PMIP3 ensemble demonstrates a 2.8° southward shift in the latitude of
246 maximum westerly wind stress in the east of the basin, but little change in the west of
247 the basin (Figure 3); this southward shift the westerly winds is in keeping with early
248 modelling work which demonstrated a southward displacement of the westerly jet
249 during the LGM (e.g. Manabe & Broccoli, 1985; Bartlein *et al.*, 1998). A southward

250 shift in the position of the easterlies – such that they blow over the northern boundary
251 of the North Pacific during the LGM, rather than over the Bering Straits and Sea as they
252 do today (Gray *et al.*, 2018) – drives a large increase in the zonal wind stress over the
253 subpolar gyre (50% increase in the west of the basin and 100% increase in the east of
254 the basin). The combined effect of the increase in easterly wind stress and the
255 southward shift and increase in westerly wind stress is a large increase in wind stress
256 curl across the subpolar gyre (Gray *et al.*, 2018), with a southward expansion in positive
257 wind stress curl in the east of the basin. This southward expansion in positive wind
258 stress curl in the east drives the southward expansion of the subpolar gyre across the
259 entire basin because the circulation is, to a good approximation, in Sverdrup balance
260 and therefore reflects the zonal integral of $\nabla \times \tau$ from the eastern boundary of the basin
261 (Sverdrup, 1947; Hautala *et al.*, 1994; Deser *et al.*, 1999; Wunsch, 2011).

262

263 To investigate which forcing(s) ultimately drive the wind stress and gyre
264 circulation changes during the LGM, we analysed HadCM3 model runs with individual
265 LGM forcings from greenhouse gases, ice sheet albedo, ice sheet topography, and
266 combined ice sheet albedo and topography (Figure 4). Substantial changes in the
267 position of $\nabla \times \tau = 0$ and $\Psi_{\text{barotropic}} = 0$ are only seen with the combined effects of ice
268 sheet topography and albedo; ice sheet topography or ice sheet albedo alone have very
269 little effect, as do greenhouse gases. This result illustrates a large non-linearity in the
270 response of atmospheric circulations to ice sheet forcing; this is the result of the distinct
271 and differing seasonality in the response of the atmosphere over the Pacific to ice sheet
272 forcing, with albedo having the greatest effect in summer and topography having the
273 greatest effect in winter (Roberts *et al.*, 2019). Note that a further shift in the gyre
274 boundary is seen with the addition of greenhouse gas forcing (Figure 4), again

275 exceeding that expected from the sum of the individual responses and suggesting a
276 further non-linear response to the combined ice sheet and greenhouse gas forcings (e.g.
277 Broccoli and Manabe, 1987).

278

279 The expansion of the subpolar gyre, and associated cold waters, drives a large
280 cooling in the mid-latitudes south of the modern-day gyre boundary. The contraction
281 and expansion of the gyre therefore act to amplify temperature changes in the mid-
282 latitudes over glacial-interglacial cycles. The strengthening of the SPG would increase
283 poleward heat transport and may play a role in driving the relative warmth of the SPG
284 during the LGM (Figure 2). A modern analogue is the Pacific Decadal Oscillation
285 ‘warm’ phase, which results from a strengthening of the subpolar gyre in response to a
286 deepening of the Aleutian Low due to stochastic fluctuations (Wills *et al.*, 2019). The
287 gyre strengthening thus acts to dampen temperature changes in the high-latitudes over
288 glacial-interglacial cycles.

289

290 The glacial increase in wind stress curl seen within the model ensemble would
291 drive a large increase in Ekman suction within the subpolar gyre (Gray *et al.*, 2018).
292 Given the close association of the wind stress curl changes driving the expansion and
293 strengthening of the subpolar gyre, we suggest that the proxy evidence for a $\sim 3^\circ$
294 southward shift in the gyre boundary is also indirect evidence for a glacial increase in
295 Ekman suction within the subpolar gyre. The impact of this increased Ekman suction
296 on surface ocean nutrients and CO₂ over deglaciation is discussed in detail in Gray *et al.*
297 *et al.*, 2018. Increased Ekman suction would also increase the salinity of the SPG with
298 increased upwelling of salty subsurface waters (e.g. Warren, 1983). Furthermore, both
299 the strengthening of the gyre circulation (via increased eddy transport from the salty

300 STG gyre and the reduced residence time of water in the SPG; Emile-Geay *et al.*, 2003)
301 and the reorganisation of the atmosphere (lower precipitation in the SPG due to the
302 southward shift in the jet stream and atmospheric river events e.g. Laine *et al.* 2009;
303 Lora *et al.*, 2017) would increase the salinity of the SPG. The reorganisation of the
304 atmosphere and gyre circulation in response to ice sheet forcing may therefore play an
305 important role in pre-conditioning basin for the enhanced overturning circulation
306 observed within the North Pacific during glacial periods (e.g. Keigwin, 1998;
307 Matsumoto *et al.*, 2002; Knudson and Ravelo, 2015; Max *et al.*, 2017), and points
308 towards a weakening of the North Pacific halocline, rather than a strengthening, under
309 glacial climates (c.f. Haug *et al.*, 1999).

310

311 3.3 Deglaciation

312 Considering all of the $\delta^{18}\text{O}$ data from east and west of 180° together, our
313 reconstruction shows the gyre boundary begins to migrate northward beginning at ~17-
314 16 ka, during Heinrich Stadial 1 (HS1) (Fig. 5d). The boundary then appears relatively
315 constant during the Bølling-Allerød (14.8-12.9 ka; B/A) with a second major shift north
316 at ~12 ka, during the latter part of the Younger Dryas. There is reasonable agreement
317 between the timing of the gyre migration in the data and the deglacial model runs, which
318 show the majority of the change occurring between ~16.5-12 ka (Fig. 5e); however, the
319 model shows a steady change, rather than the two-step change in the data. We speculate
320 this is a due to the lack of routed freshwater into the North Atlantic within these model
321 runs, via its effects on hemispheric temperature asymmetry through heat transport. The
322 timing also agrees with evidence of lake level changes in western North America (Fig.
323 5c; see below) and other Pacific-wide changes in atmospheric circulation during the
324 deglaciation (Russell *et al.*, 2014; McGee *et al.*, 2014; Jones *et al.*, 2018).

325

326 However, assessing the $\delta^{18}\text{O}$ data from the east and west of the basin separately
327 reveals a large difference in timing; the majority of the change occurs earlier in the
328 deglaciation in the east of the basin ($\sim 16.5\text{-}14$ ka) whereas the majority of the change
329 occurs later in the deglaciation in the west of the basin ($\sim 12.5 - 10.5$ ka). This east-west
330 difference in timing can be seen in the raw $\delta^{18}\text{O}_{\text{calcite}}$ data (Figure 1) and is too large to
331 be explained by age model uncertainty. Contrary to the data, HadCM3 shows no
332 difference in the timing of the northward shift of the gyre boundary between the east
333 and west, although the weakening of the westerlies does occur substantially later in the
334 west of the basin (compared to the east) within the model (Fig. 5g).

335

336 The northward migration of the gyre boundary in the east of the basin beginning
337 at ~ 16.5 ka indicates the westerly winds in the east of the basin began to shift northward
338 at this time, concomitant with the recession of the Laurentide Ice Sheet (Lambeck *et al.*,
339 2014). Such a change in atmospheric circulation within the east of the basin at this
340 time is in good agreement with records of hydroclimate in southwestern North America
341 (Figure 5c; Bartlein *et al.*, 1998; Lyle *et al.*, 2012; Ibarra *et al.*, 2014; McGee *et al.*,
342 2015; Oviatt, 2015; Lora *et al.*, 2016; Shuman & Serravezza, 2017; Bhattacharya *et al.*,
343 2018; McGee *et al.*, 2018), and suggests a clear role for dynamics in driving the
344 observed changes in hydroclimate. However, given Sverdrup balance, changes in wind
345 stress curl within the east of the basin should propagate across the basin and drive
346 changes in the position of the gyre boundary in the west, and, as noted above, only a
347 small change is seen in the west of the basin at this time.

348

349 One possible dynamical explanation for the observed difference in the timing
350 between the east and west of the basin is that the jet stream became less zonal (i.e. more
351 tilted) during this period, and as such, the northward shift in the westerlies in the east
352 did not result in a substantial change to the integrated wind stress curl across the basin,
353 resulting in a less zonal (i.e. more tilted) gyre. A more tilted jet stream does not seem
354 unreasonable given the large changes in the size of the North American ice sheets
355 beginning at this time (e.g. Lambeck *et al.*, 2014), and is in good agreement with
356 terrestrial proxy records and paleoclimatic simulations of this time period (Wong *et al.*,
357 2016; Lora *et al.*, 2016). Increased heat transport from a more tilted gyre could help
358 explain the anomalous warmth of the SPG during the Bølling-Allerød (e.g. Gray *et al.*,
359 2018), and may help drive wider northern-hemisphere warming at this time. We note
360 that the tilt of the gyre in the modern North Atlantic is poorly simulated by climate
361 models (Zappa *et al.*, 2013), and thus it may also be poorly simulated in the North
362 Pacific. We also note the other models (besides HadCM3) better simulate the larger
363 gyre boundary shift in the east relative to the west under glacial forcing (Fig. 4c), and
364 thus may better simulate gyre tilt.

365

366 **6. Conclusions**

367 Using a basin wide compilation of planktic foraminiferal $\delta^{18}\text{O}$ data we show
368 that the boundary between the North Pacific subpolar and subtropical gyres shifted
369 southward by $\sim 3^\circ$ during the Last Glacial Maximum, consistent with sea surface
370 temperature and productivity proxy data. This expansion of the North Pacific subpolar
371 gyre is evident within all PMIP3 climate models forced with glacial boundary
372 conditions. The models suggest that this expansion is associated with a substantial
373 strengthening of the subpolar gyre. The strengthening of the subpolar gyre is driven by

374 an increase in wind stress curl within the subpolar gyre resulting from a southward shift
375 and strengthening of the mid-latitude westerlies in the east of the basin, and a southward
376 shift in the polar easterlies across the basin. The expansion of the gyre is driven by a
377 southward expansion of the area of positive wind stress curl within the east of the basin,
378 due to the southward shift in the westerlies. Using model runs with individual forcings,
379 we demonstrate that the changes in wind stress curl and associated expansion and
380 strengthening of the subpolar gyre are a response to the combined effects of ice sheet
381 albedo, ice sheet topography, and CO₂. Changes are small in climate model simulations
382 where albedo and topography are forced separately, compared to their combined
383 effects, illustrating the highly non-linear nature of the response of atmospheric
384 circulation to ice sheet forcing (e.g. Löffverström *et al.*, 2014; Roberts *et al.*, 2019).

385

386 The southward expansion of the subpolar gyre would have brought nutrient-rich
387 waters further south, explaining why productivity increased in the transition zone
388 between the gyres while decreasing throughout the subpolar gyre during LGM. The
389 expansion and contraction of the subpolar gyre acts as a mechanism to amplify
390 temperature changes in the mid-latitudes over glacial-interglacial cycles. On the
391 contrary, the strengthening of the subpolar gyre would increase poleward heat transport,
392 warming the north of the basin and dampening temperature changes in the high-
393 latitudes over glacial-interglacial cycles. The strengthening of the gyre circulation, in
394 conjunction with increased Ekman suction (Gray *et al.*, 2018), and reduced
395 precipitation (Lora *et al.*, 2017), would also make the subpolar gyre saltier, weakening
396 the halocline under glacial climates (c.f. Haug *et al.*, 1999).

397

398 Our gyre-boundary reconstruction offers a constraint on the position of the mid-
399 latitude westerly winds over the last deglaciation and suggests the westerly winds began
400 to shift northward at ~17-16 ka, during Heinrich Stadial 1, as the Laurentide Ice Sheet
401 receded. This reorganisation of atmospheric circulation likely drove the large changes
402 in hydroclimate within southwestern North America (e.g. Lora *et al.*, 2016), and may
403 be related to other changes in atmospheric circulation seen at this time across the whole
404 Pacific, deep into the tropics and the Southern Hemisphere (e.g. D’Agostino *et al.*,
405 2017; Jones *et al.*, 2018).

406

407 **Acknowledgments**

408 We are grateful to Lloyd Keigwin for imparting the wisdom ‘If the signal is big enough,
409 you’ll see it in the $\delta^{18}\text{O}$ of calcite’. We acknowledge the World Climate Research
410 Programme’s Working Group on Coupled Modelling for the coordination of CMIP and
411 thank the climate modelling groups for producing and making available their model
412 output (<https://esgf-node.llnl.gov/search/cmip5/>). Insightful and constructive
413 comments from two anonymous reviewers very much improved a previous version of
414 this manuscript. WRG, JWBR and AB were funded Natural Environment Research
415 Council (NERC) grant NE/N011716/1 awarded to JWBR and AB. RCJW was funded
416 by the Tamaki Foundation, NASA (Grant NNX17AH56G), and NSF (Grant AGS-
417 1929775). RFI was funded by a NERC Independent Research Fellowship
418 NE/K008536/1. The planktic foraminiferal $\delta^{18}\text{O}$ compilation used in this study will be
419 available on Pangea.

420

421 **References**

422 Bartlein, P.J., Anderson, K.H., Anderson, P.M., Edwards, M.E., Mock, C.J.,
423 Thompson, R.S., Webb, R.S., Webb, T., Whitlock, C., 1998. Paleoclimate
424 simulations for North America over the past 21,000 years; features of the simulated

425 climate and comparisons with paleoenvironmental data. *Quaternary Science*
426 *Reviews* 17, 549-585.

427 Boyer, T.P., Antonov, J.I., Baranova, O.K., Coleman, C., Garcia, H.E., Grodsky, A.,
428 John- son, D.R., Locarnini, R.A., Mishonov, A.V., O'Brien, T.D., Paver, C.R.,
429 Reagan, J.R., Seidov, D., Smolyar, I.V., Zweng, M.M., 2013. World Ocean Database
430 2013. In: Levitus, Sydney (Ed.), Alexey Mishonov (Technical Ed.), NOAA Atlas
431 NESDIS, vol. 72. 209 pp.

432 Braconnot, P., Harrison, S.P., Kageyama, M., Bartlein, P.J., Masson-Delmotte, V.,
433 Abe-Ouchi, A., Otto-Bliesner, B. and Zhao, Y., 2012. Evaluation of climate models
434 using palaeoclimatic data. *Nature Climate Change*, 2(6), 417-424.

435 Broccoli, A.J., Manabe, S., 1987. The influence of continental ice, atmospheric CO₂,
436 and land albedo on the climate of the last glacial maximum. *Climate Dynamics* 1,
437 87-99.

438 D'Agostino, R., P. Lionello, O. Adam, and T. Schneider (2017), Factors controlling
439 Hadley circulation changes from the Last Glacial Maximum to the end of the 21st
440 century. *Geophysical Research Letters* 44, 8585-8591. doi:10.1002/2017GL074533.

441 Deser, C., Alexanders, M. A., Timlin, M. S., 1999. Evidence for a Wind-Driven
442 Intensification of the Kuroshio Current Extension from the 1970s to the 1980s.
443 *Journal of Climate* 12, 1697-1706.

444 Emile-Geay, J., Cane, M.A., Naik, N., Seager, R., Clement, A.C., van Geen, A. (2003)
445 Warren revisited: Atmospheric freshwater fluxes and 'Why is no deep water formed
446 in the North Pacific'. *Journal of Geophysical Research* 108,
447 doi:10.1029/2001JC001058.

448 Forget, G, Ferreira, D, 2019. Global ocean heat transport dominated by heat export
449 from the tropical Pacific. *Nature Geoscience*, [https://doi.org/10.1038/s41561-019-](https://doi.org/10.1038/s41561-019-0333-7)
450 0333-7,

451 Gray, W.R., Rae, J.W.B, Wills, R.C.J., Shevenell, A.E., Taylor, B., Burke, A., Foster,
452 G.L., Lear, C.H., 2018. Deglacial upwelling, productivity and CO₂ outgassing in the
453 North Pacific Ocean. *Nature Geoscience* 11, 340–344.

454 Haug, G.H., Sigman, D.M., Tiedemann, R., Pedersen, T.F., Sarnthein M., 1999. Onset
455 of permanent stratification in the subarctic Pacific Ocean. *Nature* 40, 779-782.

456 Huatala, S.L., Roemmich, D.H., Schmitz, W.J., 1994. Is the North Pacific in Sverdrup
457 balance along 24°N? *Journal of Geophysical Research* 99, 16041-16052.

458 Ibarra, D. E., A. E. Egger, K. L. Weaver, C. R. Harris, and K. Maher, 2014: Rise and
459 fall of late Pleistocene pluvial lakes in response to reduced evaporation and
460 precipitation: Evidence from Lake Surprise, California. *Geol. Soc. Amer. Bull.*, 126,
461 1387–1415, <https://doi.org/10.1130/B31014.1>.

462 Ivanovic, R.F., Gregoire, L.J., Kageyama, M., Roche, D.M., Valdes, P.J., Burke, A.,
463 Drummond, R., Peltier, W.R., Tarasov, L., 2016. Transient climate simulations of
464 the deglaciation 21–9 thousand years before present (version 1) PMIP4 Core
465 experiment design and boundary conditions. *Geosci. Model Dev.* 9, 25632587.
466 <https://doi.org/10.5194/gmd-9-2563-2016>.

467 Jones, T.R., Roberts, W.H.G., Steig, E.J., Cuffey, K.M., Markle, B.R., White, J.W.C
468 (2018) Southern Hemisphere climate variability forced by Northern Hemisphere ice-
469 sheet topography. *Nature* **554**, 351-355.

470 Keigwin, L., 1998. Glacial-age hydrography of the far northwest Pacific Ocean.
471 *Paleoceanography* **13**, 323–339.

472 Key, R.M., Olsen, A., van Heuven, S., Lauvset, S.K., Velo, A., Lin, X., Schirnack, C.,
473 Kozyr, A., Tanhua, T., Hoppema, M., Jutterström, S., Steinfeldt, R., Jeansson, E.,
474 Ishi, M., Perez, F.F., Suzuki, T., 2015. Global Ocean Data Analysis Project, Version
475 2 (GLODAPv2). ORNL/CDIAC-162, ND-P093. Carbon Dioxide Informa- tion
476 Analysis Center, Oak Ridge National Laboratory, US Department of Energy, Oak
477 Ridge, Tennessee. https://doi.org/10.3334/CDIAC/OTG.NDP093_GLODAPv2.
478 http://cdiac.ornl.gov/oceans/GLODAPv2/NDP_093.pdf.

479 Kim, S. and O’Neil, J. (1997). Equilibrium and nonequilibrium oxygen isotope effects
480 in synthetic carbonates. *Geochimica et Cosmochimica Acta* **61**, 3461–3475.

481 Kirby, M. E., S. J. Feakins, N. Bonuso, J. M. Fantozzi, and C. A. Hiner, 2013. Latest
482 Pleistocene to Holocene hydroclimates from Lake Elsinore, California, *Quat. Sci.*
483 *Rev.*, 76, 1–15.

484 Knudson, K. P. and Ravelo, A. C., 2015. North Pacific Intermediate Water
485 circulation enhanced by the closure of the Bering Strait. *Paleoceanography* **30**,
486 PA002840.

487 Kohfeld, K. E. & Chase, Z., 2011. Controls on deglacial changes in biogenic fluxes in
488 the North Pacific Ocean. *Quat. Sci. Rev.* **30**, 3350–3363.

489 Lambeck, K., Rouby, H., Purcell, A., Sun, Y., Sambridge, M., 2014. Sea level and
490 global ice volumes from the Last Glacial Maximum to the Holocene. *Proc. Natl*
491 *Acad. Sci. USA* **111**, 15296–15303.

492 LeGrande, A.N., Schmidt, G.A., 2006. Global gridded data set of the oxygen isotopic
493 composition in seawater. *Geophys. Res. Lett.* **33**, L12604.

494 Li, C., Battisti, D.S., 2008. Reduced Atlantic Storminess during Last Glacial
495 Maximum: Evidence from a Coupled Climate Model. *Journal of Climate* **21** 3561-
496 3579. DOI: 10.1175/2007JCLI2166.1.

497 Lora, J. M., J. L. Mitchell, Tripathi, A. E., 2016. Abrupt reorganization of North Pacific
498 and western North American climate during the last deglaciation, *Geophys. Res.*
499 *Lett.*, 43, 11,796–11,804, doi:10.1002/2016GL071244.

500 Lora, J. M., 2018. Components and Mechanisms of Hydrologic Cycle Changes over
501 North America at the Last Glacial Maximum. *Journal of Climate* **31**, 7035-7051.

502 Löffverström, M., R. Caballero, J. Nilsson, Kleman, J., 2014. Evolution of the large-
503 scale atmospheric circulation in response to changing ice sheets over the last glacial
504 cycle. *Climate of the Past* **10**, 1453-1471.

505 Lyle, M., Heusser, L., Ravelo, C., Yamamoto, M., Barron, J., Diffenbaugh, N. S.,
506 Herbert, T., Andreasen, D., 2012. Out of the Tropics: The Pacific, Great Basin
507 Lakes, and Late Pleistocene Water Cycle in the Western United States. *Science*, **337**,
508 1629-1633.

509 Lynch-Stieglitz, J., Curry, W.B., Slowey, N. (1999) Weaker Gulf Stream in the Florida
510 Straits during the Last Glacial Maximum. *Nature* **402**, 644-648.

511 Manabe, S., Broccoli, A.J., 1985. The influence of Continental Ice Sheets on the
512 Climate of an Ice Age. *Journal of Geophysical Research* 90, 2167-2190.

513 Marcott, S.A. *et al.*, 2014. Centennial-scale changes in the global carbon cycle during
514 the last deglaciation. *Nature* **514**, 617-619. doi:10.1038/nature13799

515 Matsumoto, K., Oba, T. & Lynch-Stieglitz, J., 2002. Interior hydrography and
516 circulation of the glacial Pacific Ocean. *Quat. Sci. Rev.* **21**,1693–1704.

517 Max, L., Rippert, N., Lembke-Jene, L., Mackensen, A., Nürnberg, D., Tiedemann, R.,
518 2017. Evidence for enhanced convection of North Pacific Intermediate Water to the
519 low-latitude Pacific under glacial conditions. *Paleoceanography* **32**, 41–55.

520 McGee, D., Quade, J., Edwards, R.L, Broecker, W.S., Cheng, H., Reiners, P.W.,
521 Evenson, N., 2012. Lacustrine cave carbonates: Novel archives of paleohydrologic
522 change in the Bonneville Basin (Utah, USA). *Earth and Planetary Science Letters*
523 **351-352**, 182-194.

524 McGee, D., Donohoe, A., Marshall, J., Ferreira, D. (2014) Changes in ITCZ location
525 and cross-equatorial heat transport at the Last Glacial Maximum, Heinrich Stadial
526 1, and the mid-Holocene. *Earth and Planetary Science Letters* **390**, 69-79.

527 McGee, D., Moreno-Chamarro, E., Marshall, J., Galbraith, E.D. (2018) Western U.S.
528 lake expansions during Heinrich stadials linked to Pacific Hadley circulation.
529 *Science Advances* 4, eaav0118.

530 Morris, P.J., Swindles, G.T., Valdes, P.J., Ivanovic, R.F., Gregoire, L.J., Smith, M.W.,
531 Tarasov, L., Haywood, A.M., Bacon, K.L., 2018. Global peatland initiation driven
532 by regionally asynchronous warming. *PNAS* 201717838.
533 <https://doi.org/10.1073/pnas.1717838115>.

534 Nelson, S.T., Wood, M.J., Mayo, A.L., Tingey, D.G., Eggett, D., 2005. Shoreline tufa
535 and tufaglomerate from Pleistocene Lake Bonneville, Utah, USA: stable isotopic
536 and mineralogical records of lake conditions, processes, and climate. *Journal of*
537 *Quaternary Science* **20**, 3–19.

538 Okazaki, Y., Timmermann, A., Menviel, L., Harada, N., Abe-Ouchi, A., Chikamoto,
539 M., Mouchet, A., and Asahi, H., 2010. Deepwater Formation in the North Pacific
540 During the Last Glacial Termination. *Science* **329**, 200-204.

541 Oster, J.L., Ibarra, D.E., Winnick, M.J., Maher, K., 2015. Steering of westerly storms
542 over western North America at the Last Glacial Maximum. *Nature Geoscience* **8**,
543 201-205.

544 Oviatt, C. G., R. S. Thompson, D. S. Kaufman, J. Bright, and R. M. Forester, 1999.
545 Reinterpretation of the Burmester Core, Bonneville Basin, Utah, *Quat. Res.*, 52,
546 180–184.

547 Oviatt, C. G., 2015. Chronology of Lake Bonneville, 30,000 to 10,000 yr B.P.
548 *Quaternary Science Reviews* 110, 166-171.

549 Pausata, F. S. R., Li, C., Wettstein, J. J., Kageyama, M., and Nisancioglu, K. H., 2011.
550 The key role of topography in altering North Atlantic atmospheric circulation during
551 the last glacial period, *Clim. Past* **7**, 1089-1101, [https://doi.org/10.5194/cp-7-1089-](https://doi.org/10.5194/cp-7-1089-2011)
552 2011.

553 Rae, J. W. B., Sarnthein, M., Foster, G. L., Ridgwell, A., Grootes, P. M., and Elliott,
554 T., 2014. Deep water formation in the North Pacific and deglacial CO₂ rise.
555 *Paleoceanography* **29**, 645–667.

556 Roberts, W. H. G., Valdes, P. J., 2017. Green Mountains and White Plains: The Effect
557 of Northern Hemisphere Ice Sheets on the Global Energy Budget. *Journal of Climate*
558 **30**, 3887- 3905. DOI: 10.1175/JCLI-D-15-0846.1.

559 Roberts, W.H.G., Li, C., Valdes, P.J., 2019. The mechanisms that determine the
560 response of the Northern Hemisphere’s stationary waves to North American ice
561 sheets. *Journal of Climate*, <https://doi.org/10.1175/JCLI-D-18-0586.1>

562 Russell, J.M., Russell, Vogel, H., Konecky, B.L., Bijaksana, S., Huang, Y., Melles, M.,
563 Wattrus, N., Costa, K., King, J.W., 2014. Glacial forcing of central Indonesian
564 hydroclimate since 60,000 yr BP. *Proc. Natl Acad. Sci. USA* **111**, 5100–5105.

565 Sawada, K. and Handa, N., 1998. Variability of the path of the Kuroshio ocean current
566 over the past 25,000 years. *Nature* **392**, 592–595.

567 Schrag, D. P., Adkins, J. F., McIntyre, K., Alexander, J. L., Hodell, D. A., Charles, C.
568 D. McManus, J. F., 2002. The oxygen isotopic composition of seawater during the
569 Last Glacial Maximum. *Quaternary Science Reviews* **21**, 331-342.

570 Shuman, B.N., Serravezza, M., 2017. Patterns of hydroclimatic change in the Rocky
571 Mountains and surrounding regions since the last glacial maximum. *Quaternary*
572 *Science Reviews* **173**, 58-77.

573 Sverdrup, 1947. Wind-Driven Currents in a Baroclinic Ocean; with Application to the
574 Equatorial Currents of the Eastern Pacific. *PNAS* **33**, 318–26.

575 Taylor, K. E., R. J. Stouffer, and G. A. Meehl, 2012: An overview of CMIP5 and the
576 experiment design. *Bull. Am. Meteorol. Soc.*, **93** (4), 485–498

577 Thompson and Shackleton, 1980. North Pacific palaeoceanography: late Quaternary
578 coiling variations of planktonic foraminifer *Neogloboquadrina pachyderma*. *Nature*
579 **287**, 829–833.

580 Warren, B.A. (1983) Why is no deep water formed in the North Pacific? *Journal of*
581 *Marine Research* **41**, 327-347.

582 Wills, R. C. J., Battisti, D. S., Proistosescu, C., Thompson, L., Hartmann, D. L., &
583 Armour, K. (2019). Ocean circulation signatures of North Pacific decadal
584 variability. *Geophysical Research Letters*, **46**.
585 <https://doi.org/10.1029/2018GL080716>

586 Wong, C. I., G. L. Potter, I. P. Montañez, B. L. Otto-Bliesner, P. Behling, and
587 J. L. Oster (2016), Evolution of moisture transport to the western U.S. during the last
588 deglaciation, *Geophys. Res. Lett.*, **43**, 3468–3477, doi:10.1002/2016GL068389.

589 Wood, S.N. (2011) Fast stable restricted maximum likelihood and marginal likelihood
590 estimation of semiparametric generalized linear models. *Journal of the Royal*
591 *Statistical Society (B)* **73**, 3-36.

592 Wood, S.N., Pya N., Säfken, B. (2016) Smoothing Parameter and Model Selection for
593 General Smooth Models, *Journal of the American Statistical Association*, **111**:516,
594 1548-1563, DOI: 10.1080/01621459.2016.1180986

595 Wunsch, C., 2011. The decadal mean ocean circulation and Sverdrup balance. *Journal*
596 *of Marine Research* **69**, 417-434.

597 Zappa, G., L.C. Shaffrey, and K.I. Hodges (2013) The Ability of CMIP5 Models to
598 Simulate North Atlantic Extratropical Cyclones. *Journal of Climate* **26**, 5379–5396,
599 <https://doi.org/10.1175/JCLI-D-12-00501.1>

600

601

602

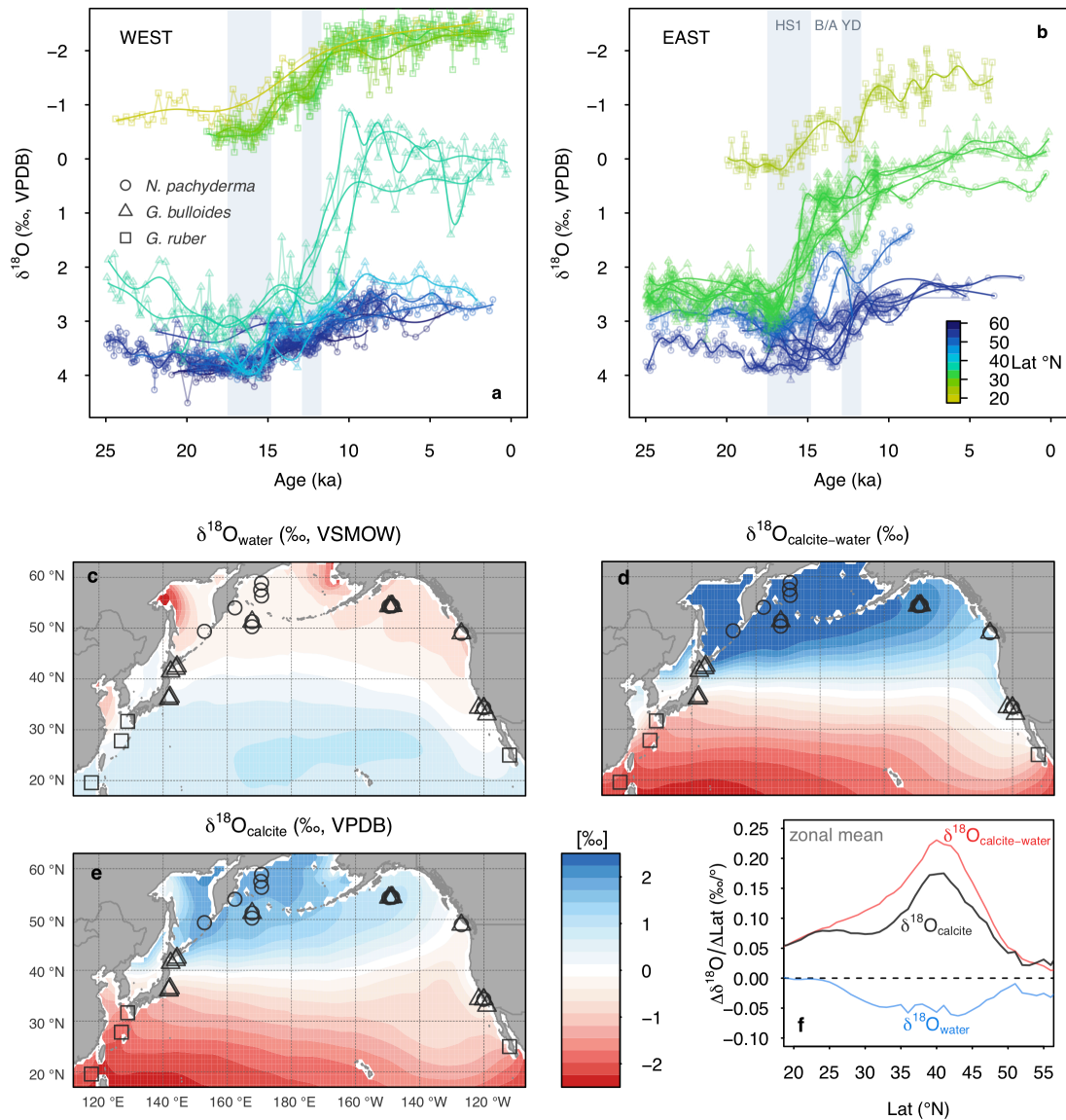
603

604

605

606

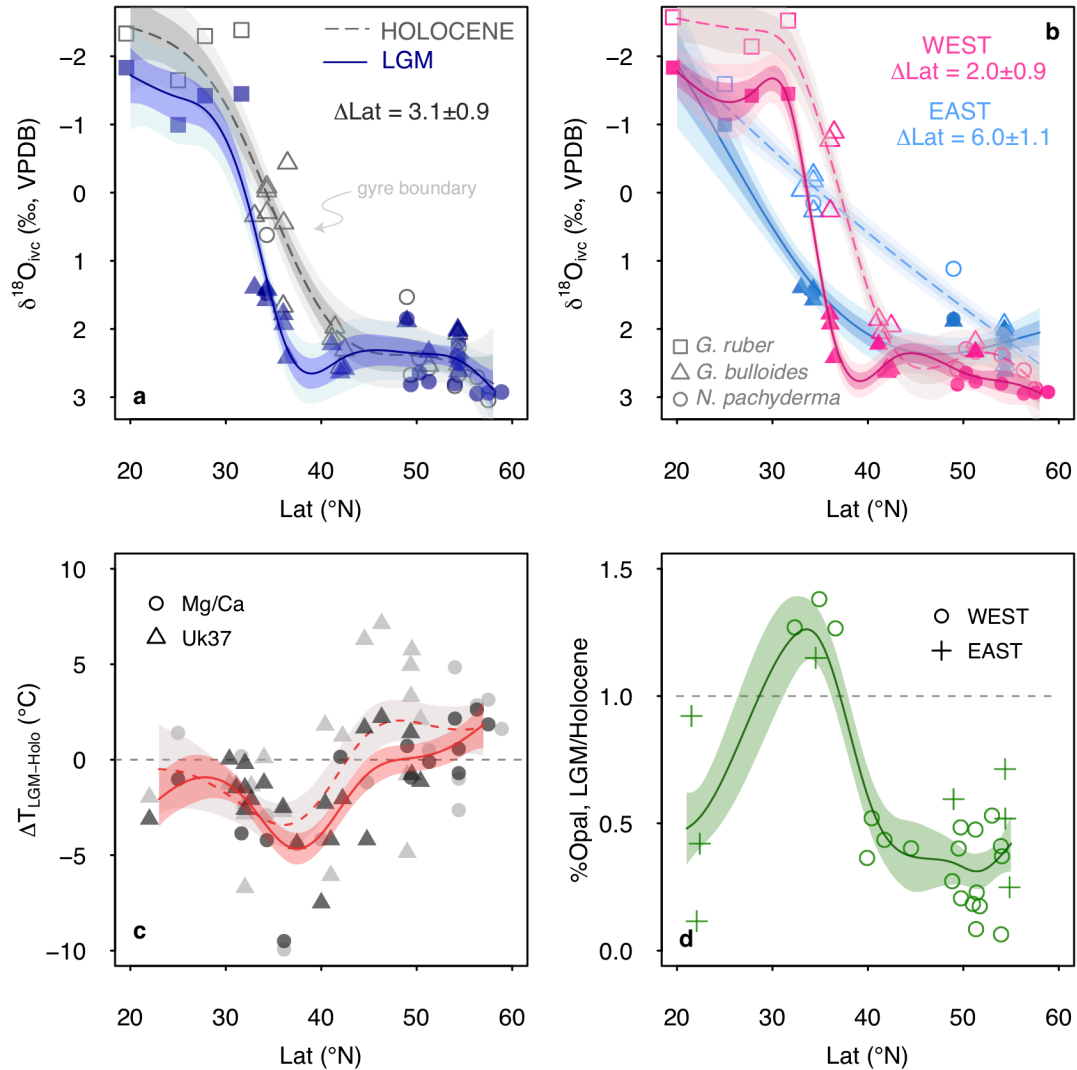
607



608

609 **Figure 1** Planktic foraminiferal $\delta^{18}\text{O}$ versus age with core site latitude represented by colour. Data are
 610 divided east (**b**) and west (**a**) of 180°. HS1, B/A and YD are Heinrich Stadial 1 (14.8-17.5 ka), Bølling-
 611 Allerød (12.9-14.8 ka) and the Younger Dryas (11.8-12.9 ka), respectively. (**c**) gridded $\delta^{18}\text{O}_{\text{water}}$ from
 612 LeGrande and Schmidt (2006) (**d**) calcite-water fractionation calculated using WOA13 mean annual
 613 temperature (Boyer et al., 2013) and the temperature-fractionation relationship of Kim and O'Neil
 614 (1997) (**e**) predicted $\delta^{18}\text{O}_{\text{calcite}}$ using (c) and (d) (note the colour scale is the same for all three panels)
 615 (**f**) slope of the zonal-mean meridional gradient in $\delta^{18}\text{O}_{\text{water}}$, $\delta^{18}\text{O}_{\text{calcite-water}}$ and $\delta^{18}\text{O}_{\text{calcite}}$. The steepest
 616 part of the meridional $\delta^{18}\text{O}_{\text{calcite}}$ gradient is lies at the gyre boundary, and is a result of the large
 617 temperature difference between the gyres.

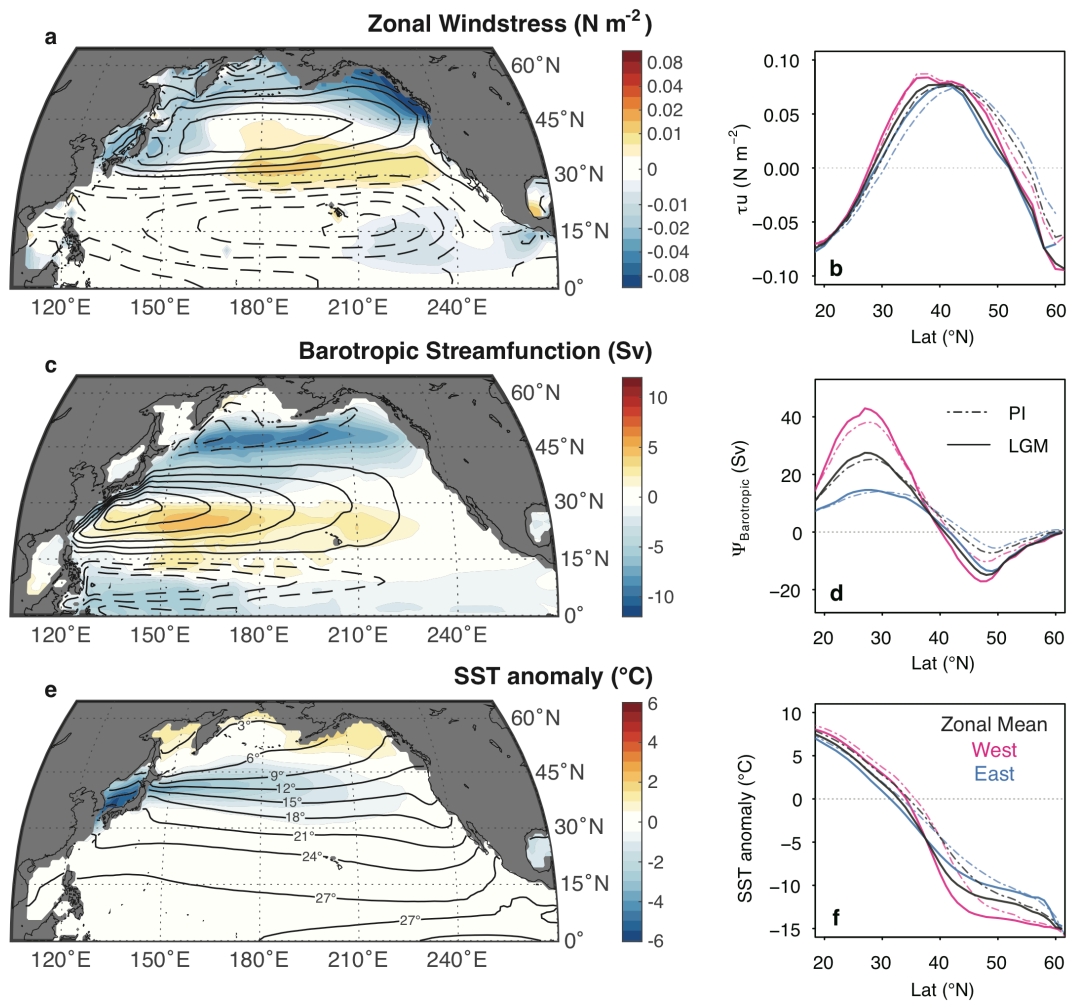
618



619

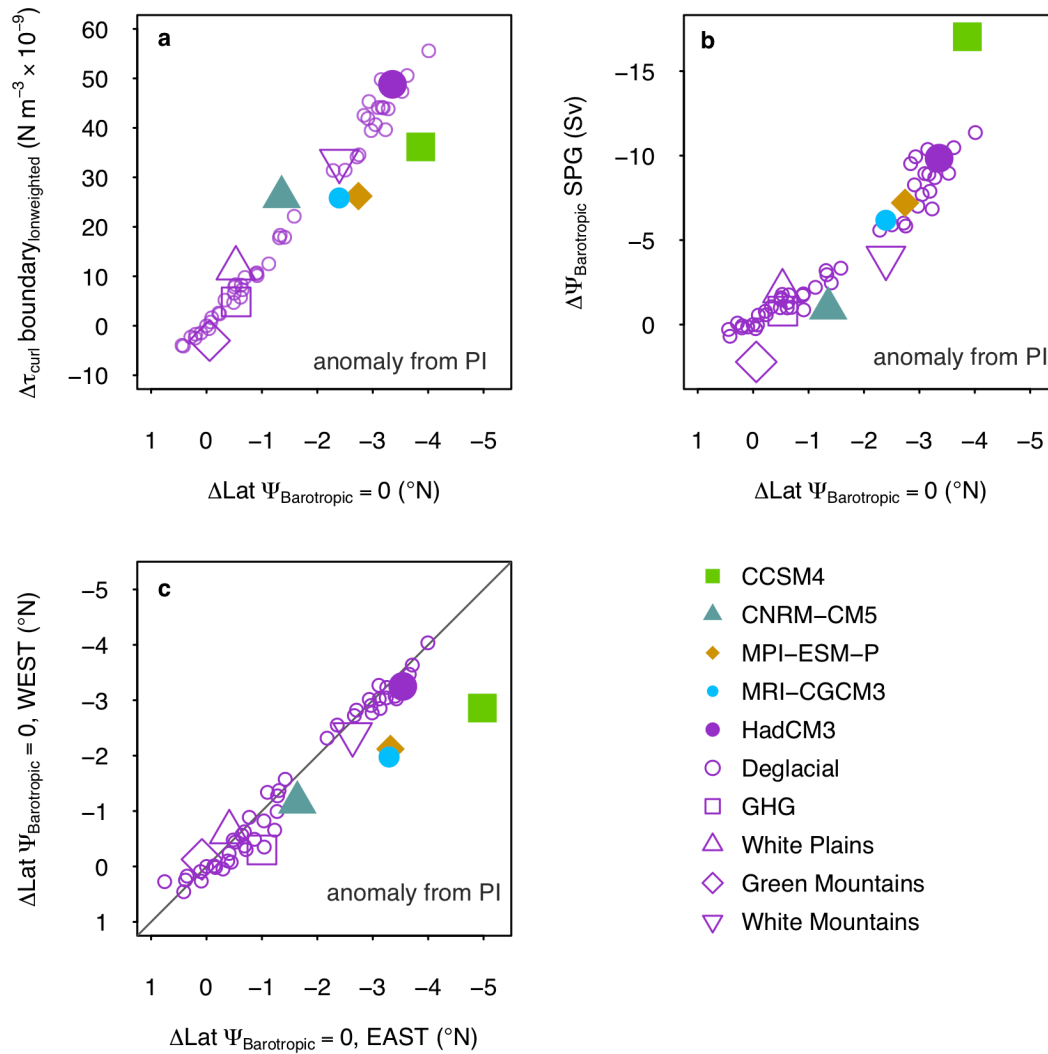
620 **Figure 2 (a)** Holocene (open symbols, dashed line) and LGM (filled symbols, solid line) foraminiferal
 621 $\delta^{18}\text{O}$ data versus latitude – symbols reflect species of planktic foraminifera (see panel b). Foraminiferal
 622 $\delta^{18}\text{O}$ values have been corrected for whole ocean changes in $\delta^{18}\text{O}_{\text{water}}$ due to changes in terrestrial ice
 623 volume and the mean ocean change in SST from the PMIP3 ensemble ($\delta^{18}\text{O}_{\text{ivc}}$; see Methods). The data
 624 are fit with a general additive model (see Methods), with the standard error (68% and 95%) of the fit
 625 shown **(b)** as in (a), however with data separated east and west of 180° **(c)** Compiled LGM-Holocene
 626 SST differences versus latitude, based on Mg/Ca and $\text{U}^{\text{k}37}$: Open symbols/dashed line is LGM proxy
 627 SST minus modern climatological SST. Filled symbols/solid line is LGM proxy SST minus Holocene
 628 proxy SST **(d)** Compiled %Opal from Kohfeld and Chase (2011) data, shown as a ratio of
 629 LGM/Holocene versus latitude, with a value of greater than 1 indicating a glacial increase. In (c) and (d)
 630 the data are fit with a general additive model, with the standard error of fit (68%) shown.

631



632

633 **Figure 3** PMIP3 ensemble mean of **(a)** LGM-PI zonal windstress (τ), with the PI climatology indicated
 634 by contours (contour interval of 0.04 N m^{-2} ; dashed is negative and solid is positive), **(b)** zonal average
 635 and averages east and west of 180° of zonal windstress in LGM and PI, **(c)** LGM-PI barotropic
 636 streamfunction ($\Psi_{\text{barotropic}}$), with the PI climatology indicated by contours (contour interval of 10 Sv ;
 637 dashed is negative and solid is positive), **(d)** zonal average and averages east and west of 180° of the
 638 barotropic streamfunction in LGM and PI **(e)** LGM-PI SST anomaly from global mean, with the PI
 639 climatology indicated by the contours **(f)** zonal average and averages east and west of 180° of the SST
 640 anomaly from global mean in the LGM and PI.



641

642 **Figure 4 (a)** LGM-PI change in latitude of zonal-mean $\Psi_{\text{barotropic} = 0}$ versus change in longitudinally
 643 weighted mean $\nabla \times \tau$ (τ_{curl}) across the southern boundary of the subpolar gyre (38-50 °N) **(b)** LGM-PI
 644 change in latitude of zonal mean $\Psi_{\text{barotropic} = 0}$ versus change in $\Psi_{\text{barotropic}}$ within the subpolar gyre
 645 (maximum north of 40°) **(c)** LGM-PI change in latitude of zonal mean $\Psi_{\text{barotropic} = 0}$ east and west of
 646 180°. Green Mountains = LGM ice sheet topography with PI albedo, White Mountains = LGM ice sheet
 647 albedo with PI topography, White Mountains = LGM ice sheet topography and albedo.

648

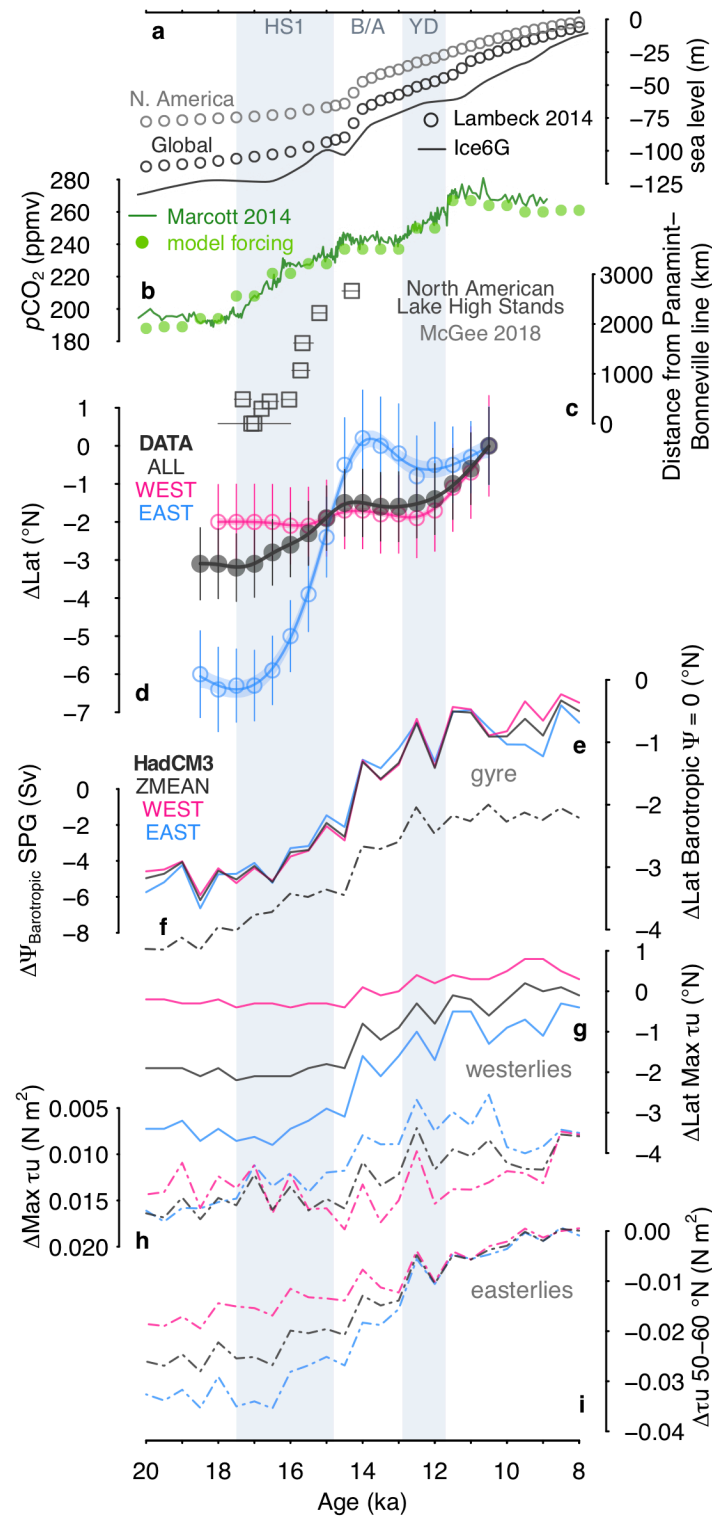
649

650

651

652

653



654

655 **Figure 5 (a)** Sealevel curve of Lambeck *et al.* (2014) and sealevel equivalent of global and
 656 American ice sheet volume in the ICE6Gc ice sheet reconstruction **(b)** Atmospheric $p\text{CO}_2$ record of
 657 Marcott *et al.* (2014) and $p\text{CO}_2$ forcing used in model **(c)** north-westward progression of lake high stands
 658 in southwestern North America (McGee *et al.*, 2018) **(d)** reconstructed change in gyre boundary position
 659 with 1σ uncertainty (east and west is east and west of 180°) **(e)** modelled change in gyre boundary

660 position **(f)** modelled change in subpolar gyre strength (maximum north of 40°) **(g)** modelled change in
661 westerly position (determined as latitude of maximum zonal windstress, τ_u) **(h)** modelled change in
662 westerly strength (determined as maximum τ_u) **(i)** modelled change in wind stress strength exerted by
663 the easterlies (determined as mean τ_u between 50-60 °N). For model results solid lines denote a change
664 in position, and the dashed lines denote a change in strength. See Figure S8 for meridional profiles of
665 (g), (h), and (i).

666

667

668

669

670

671

672

673

674

675

676

677

678

679

680

681

682

683

684

685

686

687

688

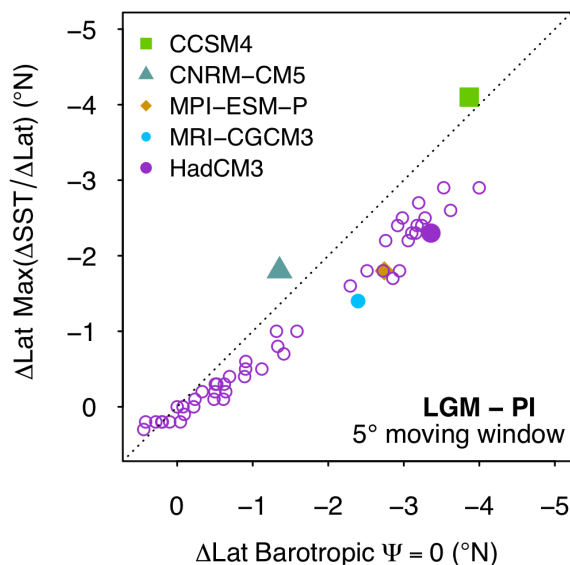
689

supporting information

690

691 *Using planktic foraminiferal $\delta^{18}\text{O}_{\text{calcite}}$ to trace the gyre boundary*

692 Our ability to use the planktic foraminiferal $\delta^{18}\text{O}_{\text{calcite}}$ to trace the gyre boundary
693 comes from the dominance of the temperature signal over that of $\delta^{18}\text{O}_{\text{water}}$ in driving
694 the meridional pattern of $\delta^{18}\text{O}_{\text{calcite}}$ across the basin; the temperature signal is ~5 times
695 greater than the $\delta^{18}\text{O}_{\text{water}}$ (~salinity) signal (Figure 1). As the spatial temperature pattern
696 across the basin is primarily governed by the gyre circulation, with the steepest
697 meridional temperature gradient (and thus meridional $\delta^{18}\text{O}_{\text{calcite}}$ gradient) at the gyre
698 boundary, we can use the meridional profiles of temperature ($\sim\delta^{18}\text{O}_{\text{calcite}}$) to track the
699 movement of the gyre boundary. Coupled climate models demonstrate a very tight
700 coupling between the LGM-PI change in latitude of gyre boundary (defined where
701 barotropic stream function = 0) and LGM-PI change in the latitude of maximum
702 latitudinal gradient in sea surface temperature (SST) (Figure S1). As no mechanism
703 exists to drive changes in $\delta^{18}\text{O}_{\text{water}}$ of the same magnitude as the changes in $\delta^{18}\text{O}_{\text{calcite-}}$
704 _{water} fractionation from the large temperature difference between the gyres (Figure 1d),
705 the temperature signal will always dominate over the $\delta^{18}\text{O}_{\text{water}}$ signal in determining the
706 spatial pattern of $\delta^{18}\text{O}_{\text{calcite}}$ (Figure 1e) across the basin and the maximum meridional
707 $\delta^{18}\text{O}_{\text{calcite}}$ gradient (Figure 1f); thus, while there are likely to be local changes in $\delta^{18}\text{O}_{\text{water}}$
708 across the basin, the steepest part of the meridional $\delta^{18}\text{O}_{\text{calcite}}$ gradient will always be
709 determined by temperature, allowing us to use meridional profiles of $\delta^{18}\text{O}_{\text{calcite}}$ to track
710 the position of the gyre boundary through time.



711

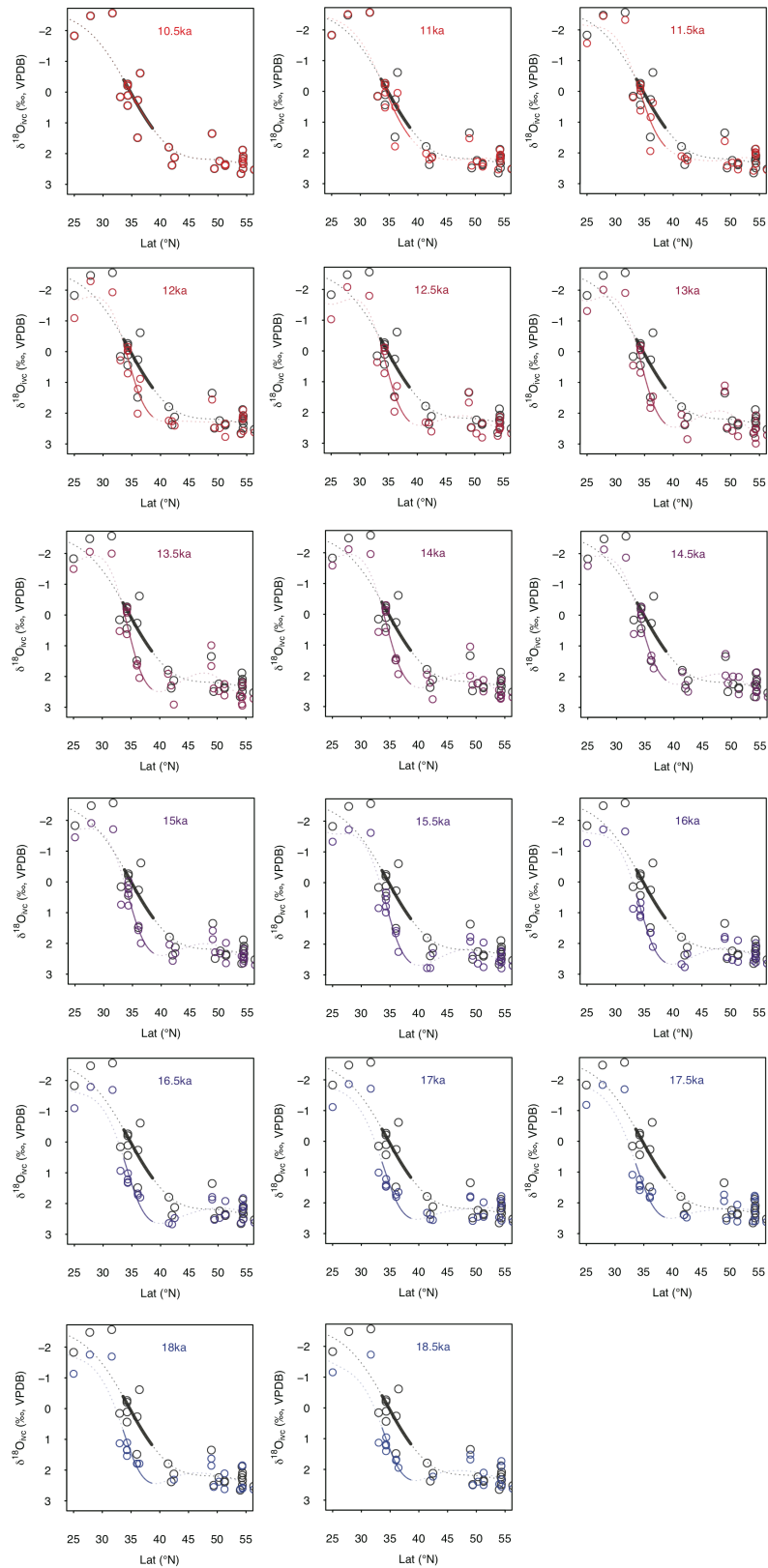
712 **Figure S1** Modelled zonal mean LGM-pre-industrial (PI) change in latitude of gyre boundary (defined
 713 where barotropic stream function = 0) versus LGM-PI change in latitude of maximum meridional
 714 gradient in sea surface temperature (SST) within a 5° moving window; the close relationship
 715 demonstrates past changes in the position of the maximum gradient in SST/Lat (and thus $\sim\delta^{18}\text{O}_{\text{calcite}}/\text{Lat}$)
 716 can be used to trace changes in the position of the gyre boundary.
 717

718 We model the $\delta^{18}\text{O}_{\text{calcite}}$ data as a function of latitude, using a general additive
 719 model (GAM) (Wood, 2011; Wood *et al.*, 2016) in the *mgcv* package in R (R core
 720 Team) at 500 yr timesteps from 18.5 to 10.5 ka (the time interval for which we have
 721 sufficient spatial and temporal resolution in our dataset; Figure 1),

$$722 \quad \delta^{18}\text{O}_{\text{calcite}} = \beta + f(\text{Lat}) + \varepsilon$$

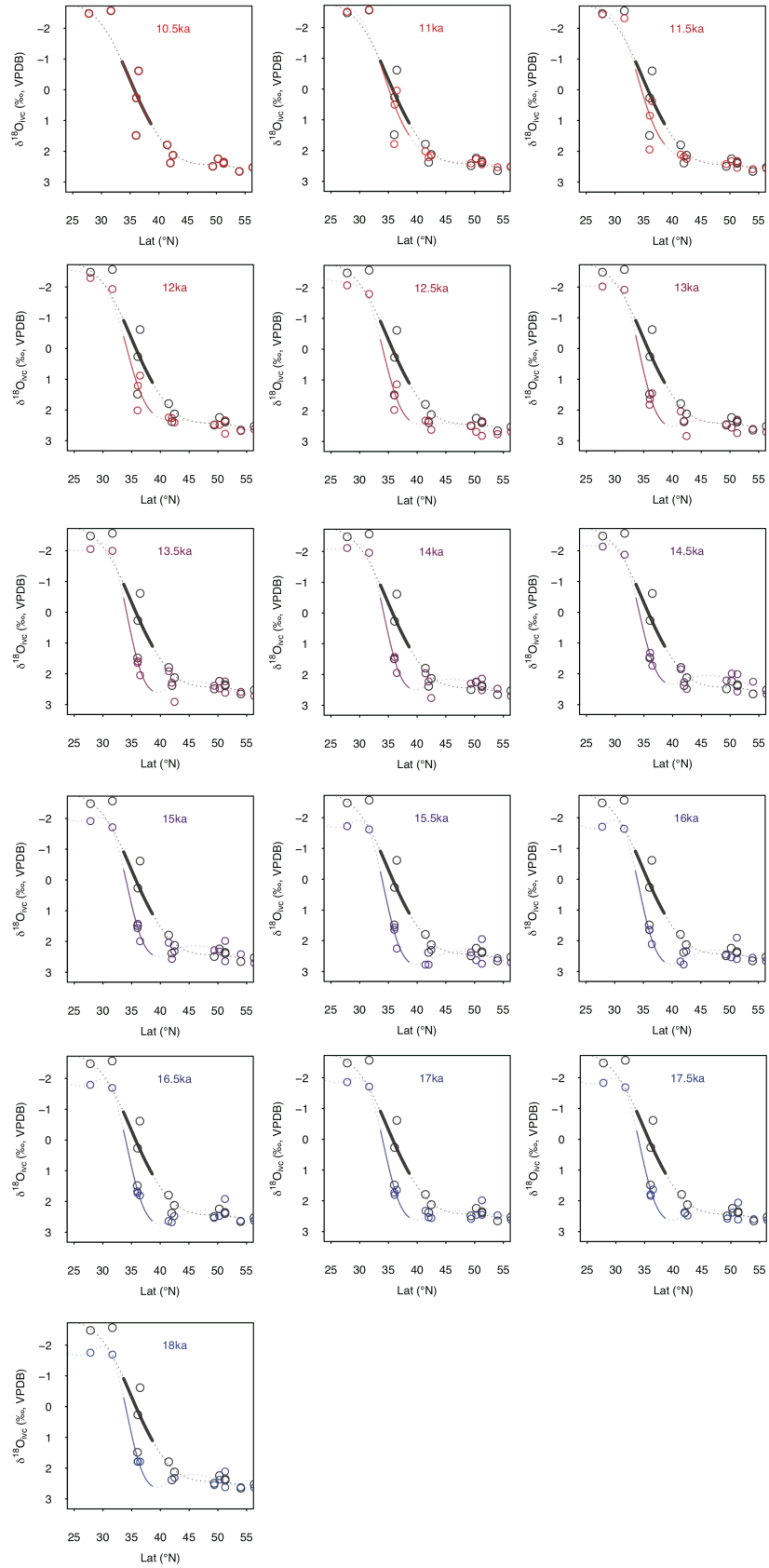
723 where $f(\text{Lat})$ is the sum of the underlying basis functions (Wood, 2011; Wood *et al.*,
 724 2016). The smoothing term (λ) was determined using generalised cross validation
 725 (GCV). We tested the models fitted using GCV by fitting models with an identical form,
 726 however using Reduced Maximum Likelihood (REML), which can sometimes be a
 727 preferable method to GCV (Reis and Ogden, 2009; Wood *et al.*, 2016), to determine
 728 the smoothing term; both GCV and REML result in identical smoothing terms, very
 729 similar degrees of freedom (4.06 with GCV versus 4.19 with REML), and
 730 indistinguishable model fits.

731



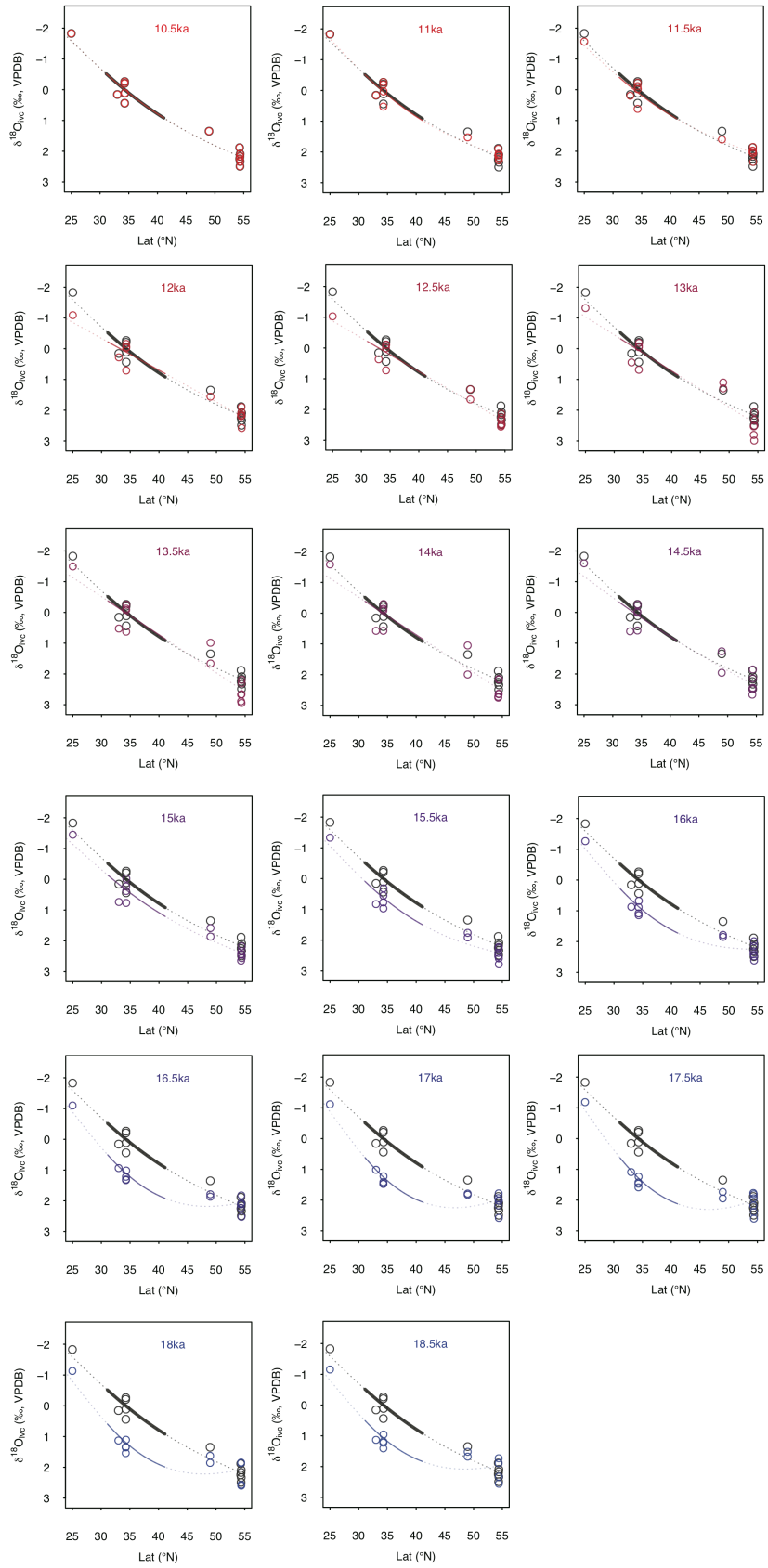
732

733 **Figure S2** GAM fits to $\delta^{18}\text{O}_{\text{calcite}}$ data as a function of latitude at 500 year timesteps from 18.5 to 10.5 ka
 734 (colours); the GAM fit to Holocene $\delta^{18}\text{O}_{\text{calcite}}$ data (10.5 ka) is shown in grey. The portion of the curve
 735 within the latitudinal band used to calculate the shift in gyre position is shown by the solid line; at each
 736 timestep we calculate the latitudinal shift that minimises the Euclidian distance between the solid part of
 737 the coloured curve and the solid part of the grey curve. Data are the combined east-west dataset (marked
 738 ALL on Figure 4).



739
740

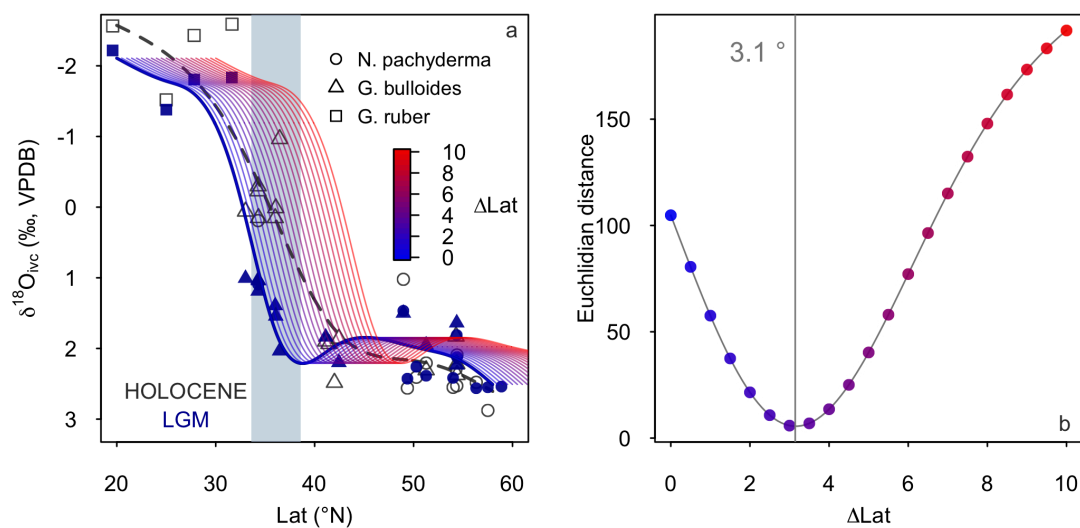
Figure S3 As figure SX, however data are from west of 180°.



741
742
743

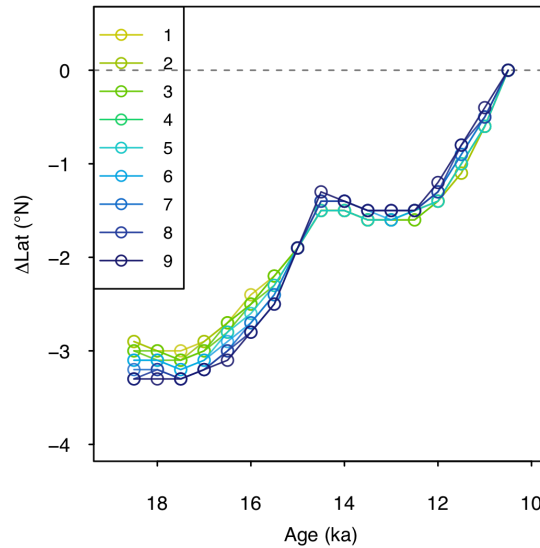
Figure S4 As figure SX, however data are from east of 180° .

744 We calculate the change in gyre boundary position over deglaciation as the
 745 latitudinal shift (x°) that minimises the Euclidian distance (L^2) between the Holocene
 746 (taken as 10.5 ± 0.5 ka) $\delta^{18}\text{O}_{\text{calcite}} \sim \text{latitude}$ GAM fit and the GAM fit to each time step,
 747 within a latitudinal band spanning the gyre boundary; this latitudinal band is centred
 748 around the maximum gradient in $\delta^{18}\text{O}_{\text{calcite}}$ versus latitude in the Holocene data within
 749 a 5° moving window (36.1°N). In the combined dataset from the east and west, and
 750 the data from the west only, we calculate the latitudinal shift using a 5° latitudinal band
 751 (i.e. 33.6 to 38.6°N), and we note the size of this latitudinal band has only a negligible
 752 effect on our results (Fig. SX); as the gyre boundary (and thus meridional temperature
 753 and $\delta^{18}\text{O}_{\text{calcite}}$ gradient) is more diffuse in the east, we use a slightly larger window of
 754 10° (i.e. 31.1 to 41.1°N).



755

756 **Figure S5** method used to calculate the shift in gyre boundary position **(a)** at each time step (here LGM,
 757 18.5 ka) we calculate the gyre boundary shift as the latitudinal shift (x° , in 0.1° increments from 0 to 10
 758 degrees) that minimises the Euclidian distance **(b)** within a specified latitudinal band (grey box in **(a)**)
 759 between the GAM fit to the timestep and the Holocene in data is calculated. The coloured lines in **(a)**
 760 show the LGM GAM fit shifted north in 0.5° increments, and the coloured dots in **(b)** show the Euclidian
 761 distance at each increment, with the colour indicating the degree to which the curve has been shifted.
 762



763

764 **Figure S6 (a)** calculated change in the position of the gyre boundary using different sizes of latitudinal
 765 band (between 1° and 9°) in which the Euclidian distance is calculated; the size of latitudinal band (the
 766 grey box in figure SXa above) has very little effect on the results.
 767

768 We note that the steepest part of the Holocene curve ($\sim 36.1^\circ\text{N}$) using the
 769 combined dataset from the east and west, is further south than the zonal mean position
 770 of the gyre boundary today ($\sim 40^\circ\text{N}$). This is due to the westward bias within the dataset
 771 (i.e. there are many more sites in the west relative to the east within the dataset), and
 772 the gyre boundary is located slightly further south in the west relative to the zonal mean;
 773 the maximum meridional gradient in mean annual SST is found at $\sim 36^\circ\text{N}$ along the
 774 western margin of the basin (Boyer et al., 2013), in good agreement with our
 775 reconstruction.

776

777 We also note that if we use a totally different method to calculate the change in
 778 position of the gyre boundary, simply calculating the change in latitude in the steepest
 779 part of the meridional $\delta^{18}\text{O}_{\text{calcite}}$ gradient (within a 5° moving window), we arrive at a
 780 very similar estimate of a $\sim 2.6^\circ$ southward shift between the Holocene and LGM. This
 781 method is more prone to anomalous values at the latitudinal extremes, hence we opt for
 782 the method of calculating the latitudinal shift that minimises the Euclidian distance

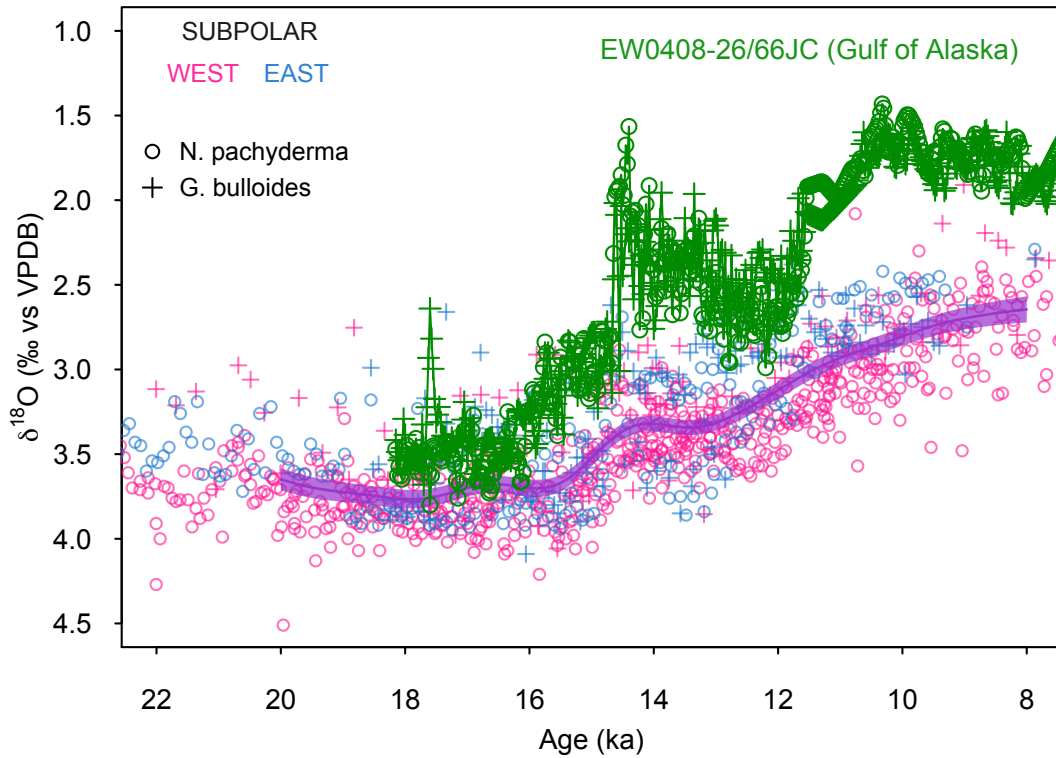
783 between timesteps within a defined latitudinal band described above; however, the
784 agreement between the two methods is reassuring.

785

786 *Planktic foraminiferal $\delta^{18}O_{\text{calcite}}$ compilation*

787 We compiled all available planktic foraminiferal calcite $\delta^{18}O$ from cores across the
788 North Pacific. All data were kept on the original age models, except in the case when
789 data were only available on uncalibrated ^{14}C age models, in which case the ^{14}C data
790 were recalibrated using INTCAL13 (Reimer et al., 2013) using an average of the
791 modern reservoir age at each site and a regional glacial increase of +400 years with
792 large uncertainties (± 500 years). All $\delta^{18}O_{\text{calcite}}$ data along with the core, location, water
793 depth, species, sediment depth, age, and original data reference are given in Table S1.

794 We only include cores spanning the interval between 10.5 to 18.5 ka with an average
795 resolution of >1 point per ka. We exclude core EW0408-26/66JC from the compilation
796 (Praetorius and Mix, 2014); this core is located in close proximity to the terminus of
797 a glacier and comparing the $\delta^{18}O_{\text{calcite}}$ data of this core to other cores within the subpolar
798 gyre demonstrates planktic foraminiferal $\delta^{18}O_{\text{calcite}}$ data from this core primarily reflect
799 local meltwater changes, rather than wider oceanographic conditions in the subpolar
800 gyre (Figure S3). The compiled dataset will be available on Pangea.



801

802 **Figure S7** Foraminiferal $\delta^{18}\text{O}_{\text{calcite}}$ from the subpolar gyre over deglaciation. A GAM fit with to all the
 803 data (excluding core EW0408-26/66JC) is shown by the purple line, with standard error of the fit shaded.
 804 Data from core EW0408-26/66JC (Praetorius and Mix, 2014) is shown in green.

805

806 *Seasonality of planktic foraminifera*

807 Our approach assumes that any change in seasonal bias relating to the habitat preference
 808 of foraminifera are small relative to the change in temperature due to the movement of
 809 the gyre boundary. The validity of this approach is supported by sites where $\delta^{18}\text{O}_{\text{calcite}}$
 810 has been measured on more than one species of foraminifera, such as core ODP Site
 811 893 (Figure 1 and Figure 2). At this site, foraminiferal species with habitat temperature
 812 preferences that are known to be different (*G. bulloides* and *N. pachyderma*, e.g. Taylor
 813 *et al.*, 2018) show very similar changes down core, with a Holocene-LGM change that
 814 is identical (within error); this suggests any changes relating to changes seasonal bias
 815 are likely to be insignificant in our reconstruction.

816

817

818 *Sea surface temperature compilation*

819 We compiled Mg/Ca and $U^{K'}_{37}$ sea surface temperature (SST) data from across the
820 North Pacific (Mg/Ca: Reitdorf et al., 2013; Gebhardt et al., 2008; Rodriguez Sanz et
821 al., 2013; Taylor et al., 2015; Sagawa et al., 2006; Sagawa et al., 2008; Pak et al., 2012;
822 Kubota et al., 2010; Gray et al., 2018. $U^{K'}_{37}$: Minoshima et al., 2007; Seki, 2004; Harada
823 et al., 2004; Harada, 2006; Harada et al., 2008; Inagaki et al., 2009; Herbert et al., 2001;
824 Sawada et al., 1998; Yamamoto et al., 2004; Isono et al., 2009). All age models are as
825 given in the original publication. All Mg/Ca and $U^{K'}_{37}$ data were recalibrated (see
826 below) and the temperature change during the LGM is given as a difference to both
827 proxy temperature in the Holocene, and to mean annual climatological temperature
828 from the WOA13 (Boyer et al., 2013).

829 While the direct temperature sensitivity of Mg/Ca in planktic foraminifera is ~6% per
830 °C (Gray et al., 2018b; Gray and Evans, 2019), due to the effect of temperature on pH
831 through the disassociation constant of water (K_w), the ‘apparent’ Mg/Ca temperature
832 sensitivity is higher (Gray et al., 2018b). Thus, we calculate the change in temperature
833 from the change in Mg/Ca at each site using a temperature sensitivity of 8.8%, derived
834 from laboratory cultures (Kisakürek et al., 2008), which encompasses both the direct
835 temperature effect and the temperature-pH effect, with a Mg/Ca-pH sensitivity of ~ -
836 8% per 0.1 pH unit (Lea et al., 1999; Russell et al., 2004; Evans et al., 2016; Gray et
837 al., 2018b; Gray and Evans, 2019). Mg/Ca is also influenced by salinity, with a
838 sensitivity of ~4% per PSU (Hönisch et al., 2013; Gray et al., 2018b; Gray and Evans,
839 2019). We make no attempt to account for the effects of salinity (due to sea level) or
840 pH downcore (due to lower atmospheric CO₂). The combined effect of the whole-ocean
841 increase in salinity (due to sea level), and the increase in surface ocean pH (due to lower
842 atmospheric CO₂) means changes in temperature derived from changes in Mg/Ca are

843 likely to be cold-biased by ~ 1.5 °C during the LGM (Gray and Evans, 2019). For UK^K₃₇,
844 the change in temperature at each site was calculated using the calibration of Prah1 et
845 al., 1988; the temperature range in this study is too low to be substantially effected by
846 the non-linearity of UK^K₃₇ (e.g. Tierney and Tingley, 2018).

847

848 *General Circulation Models*

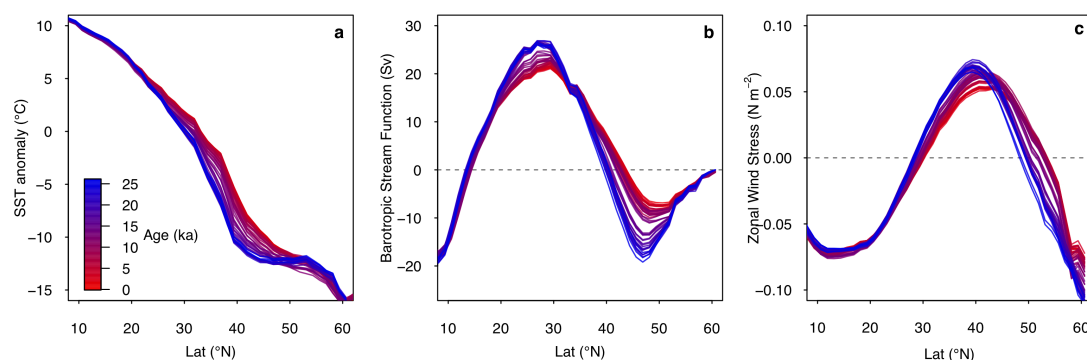
849 We assess differences in North Pacific barotropic stream function, wind stress curl,
850 zonal wind stress, and SST between LGM and pre-industrial conditions as represented
851 by five coupled climate models (CCSM4, CNRM-CM5, MPI-ESM-P and MRI-
852 CGCM3). All models are part of the Coupled Model Intercomparison Project phase 5
853 (CMIP5, Taylor et al., 2012). We only used models where both wind stress and
854 barotropic stream function data are available. Orbital parameters, atmospheric
855 greenhouse gas concentrations, coastlines and ice topography for the LGM simulations
856 are standardized as part of the Paleoclimate Model Intercomparison Project phase 3
857 (PMIP3) (Braconnot *et al.* 2012, Taylor *et al.* 2012). Ensemble means are computed by
858 first linearly interpolating to a common grid.

859

860 Using a single model (HadCM3) we look at runs where the model greenhouse gas, ice
861 sheet albedo, ice sheet topography are changed individually ('Green Mountains, White
862 Plains') as described in Roberts and Valdes (2017). The 'Green Mountains, White
863 Plains' runs use the ICE5G ice sheet reconstruction (Peltier *et al.*, 2004), whereas the
864 deglacial 'snapshot' runs (below) use the ICE6G ice sheet reconstruction (Peltier *et al.*,
865 2015).

866

867 We also explore changes through time over the deglaciation using a series of HadCM3
868 equilibrium-type simulations where all forcings and model boundary conditions are
869 changed at 500-year intervals broadly adhering to the PMIP4 last deglaciation protocol
870 (Ivanovic et al., 2016). These simulations use the ICE6GC ice sheet reconstruction and
871 'melt-uniform' scenario for ice sheet meltwater; i.e. freshwater from the melting ice
872 sheets is NOT routed to the ocean via coastal outlets. Instead, water is conserved by
873 forcing the global mean ocean salinity to be consistent with the change in global ice
874 sheet volume with respect to present. Note, these deglacial simulations are not transient,
875 but are equilibrium-type experiments that begin from the end of the 1750-year long
876 simulations run by Singarayer et al. (2011). At each 500-year interval (21.0 ka, 20.5 ka,
877 20.0 ka...0.5 ka, 0.0 ka), all boundary conditions and forcings are updated according to
878 the more recent literature (presented by Ivanovic et al., 2016) and held constant for the
879 full 500-year duration of the run. The climate means and standard deviations used here
880 are calculated from the last 50 years of each simulation (i.e. year 451-500, inclusive).
881 More information on these runs can be found in the supplement to Morris et al. (2018),
882 noting that we use the raw model output and not the downscaled and bias-corrected
883 data used in the previous publication.



884

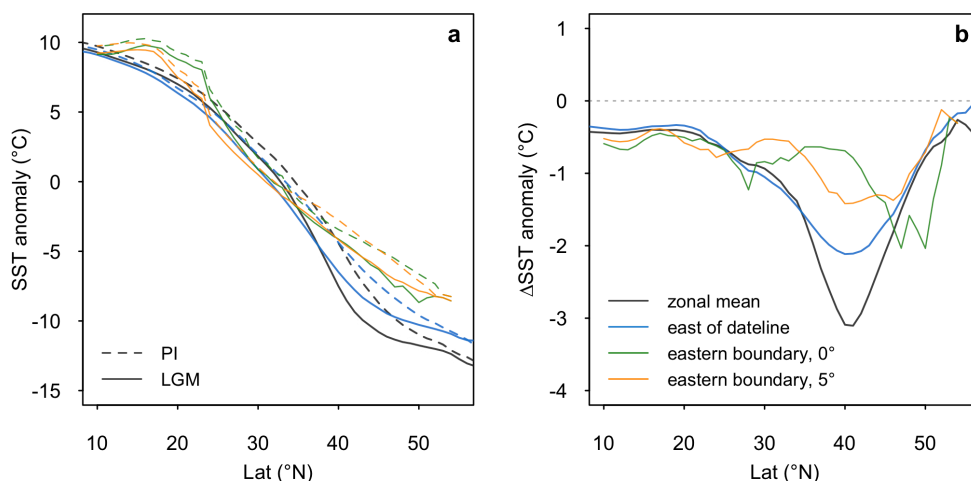
885 **Figure S8** Deglacial evolution of zonal mean (a) SST anomaly (relative to global mean) (b) barotropic
886 stream function (c) zonal wind stress in the HadCM3 simulations.

887

888

889 *Eastern boundary test*

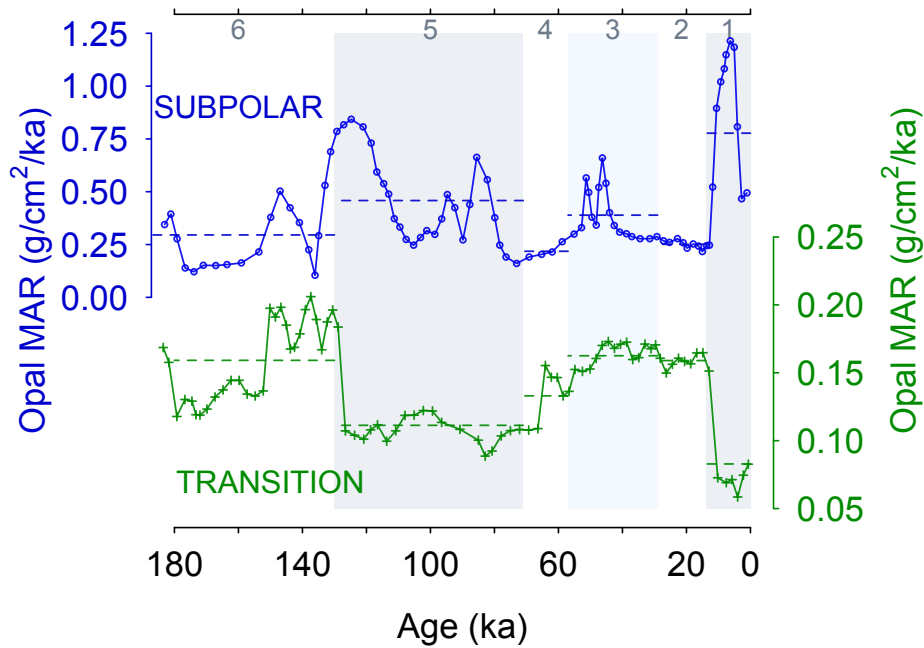
890 To test if there is an influence of coastal upwelling on the data in the east (i.e. a signal
891 of some other control on latitudinal temperature anomaly [and thus latitudinal $\delta^{18}\text{O}_{\text{calcite}}$
892 anomaly] besides change in gyre position) we compare the ensemble mean SST along
893 the eastern boundary of the basin (taken as the first oceanic grid point west of land
894 during the LGM) to the zonal mean, and zonal mean east of the dateline (Fig. S9). The
895 models show no indication of a strong influence of coastal upwelling, which would
896 manifest as an anomalous cooling relative to the zonal mean. This analysis suggests
897 coastal upwelling is unlikely to be having a significant effect on our results, although
898 the simulated coastal upwelling may be poorly represented due to the resolution of the
899 models. A further argument against a strong influence of upwelling on the data in the
900 East Pacific is that sites that are $\sim 15^\circ$ apart from each other latitudinally, such that they
901 are in different upwelling regimes today and are likely to have undergone very different
902 changes in upwelling since the LGM, display very similar patterns of change in
903 $\delta^{18}\text{O}_{\text{calcite}}$ over deglaciation, with no differences in timing (Fig. 1).



904

905 **Figure S9 (a)** LGM and PI SST anomaly (from global mean), and **(b)** LGM-PI SST anomaly in different
906 longitudinal bins; zonal mean (grey), zonal mean east of the dateline (180°, blue), along the eastern
907 boundary of the basin (green), and 5° seaward from the eastern boundary of the basin (orange). Note, the
908 gyre boundary is located slightly further north along the eastern margin relative to the zonal mean and
909 zonal mean east of the dateline.

910



911

912 **Figure S10** Opal Mass Accumulation Rate data from core KH99-03 in the SPG (Narita et al., 2002) and
 913 core NCG108 in the transition zone (Maeda et al., 2002). Dashed lines show mean value for each marine
 914 isotope stage (MIS). Grey shading shows MIS 1, 3 and 5. Transition zone and subpolar waters show an
 915 anti-phased relationship in Opal MAR over the last glacial cycle.
 916

917 *HSI Freshwater test*

918 The release of large amounts of freshwater into the eastern subpolar North Pacific has
 919 been suggested over deglaciation, at ~17.5 ka (Maier *et al* 2018). The release of
 920 freshwater into the eastern subpolar North Pacific is evident in an increase in the
 921 $\delta^{18}\text{O}_{\text{calcite}}$ difference between the mixed-layer dwelling species *G. bulloides* and the
 922 slightly deeper-dwelling species *N. pachyderma* in core MD02-2489 (54.39°N, -
 923 148.92°E) at this time; during this interval *G. bulloides* becomes ~0.6‰ more depleted
 924 than *N. pachyderma*. To test if this release of freshwater may be influencing our gyre
 925 boundary reconstruction we re-run the gyre-boundary analysis, however removing the
 926 *G. bulloides* data from core MD02-2489; the results are identical to the gyre boundary
 927 reconstruction including the *G. bulloides* data demonstrating that the effect of
 928 freshwater release has very little effect on our gyre boundary reconstruction. This is
 929 because the change in $\delta^{18}\text{O}_{\text{calcite}}$ from the freshwater release (~0.6‰, equivalent to ~2

930 PSU freshening) is very small compared to the large change in $\delta^{18}\text{O}_{\text{calcite}}$ resulting from
931 the temperature difference between the gyres (6 ‰). Localised freshwater inputs, while
932 having a large effect locally, do very little to change the pattern of $\delta^{18}\text{O}_{\text{calcite}}$ at the basin
933 scale.

934

935

936

937

938

939

940

941

942

943

944

945

946

947

948

949

950

951

952

953

954

955

956

957

958

Table S1 Compiled planktic foraminiferal $\delta^{18}\text{O}_{\text{calcite}}$ records. The compiled will be made available on Pangea.

Core	Lat (°N)	Lon (°E)	Species	Reference
MD02-2489	54.39	-148.921	N. pachyderma	Gebhardt et al 2008
MD02-2489	54.39	-148.921	G. bulloides	Gebhardt et al 2008
PAR87A-10	54.363	-148.4667	G. bulloides	Zahn et al 1991
PAR87A-10	54.363	-148.4667	N. pachyderma	Zahn et al 1991
PAR87A-02	54.29	-149.605	G. bulloides	Zahn et al 1991
PAR87A-02	54.29	-149.605	N. pachyderma	Zahn et al 1991
MD02-2496	48.967	-127.033	N. pachyderma	Taylor et al 2015
MD02-2496	48.967	-127.033	G. bulloides	Taylor et al 2015
ODP1017	34.32	-121.6	G. bulloides	Pak et al 2012
ODP893	34.2875	-120.03667	N. pachyderma	Hendy et al 2002
ODP893	34.2875	-120.03667	G. bulloides	Hendy et al 2002
MD02-2503	34.28	-120.04	G. bulloides	Hill et al 2006
AHF-28181	33.011667	-119.06	G. bulloides	Mortyn et al 1996
MD05-2505	25	-112	G. ruber	Rodríguez-Sanz et al 2013
SO201-2-101	58.883	170.683	N. pachyderma	Reitdorf et al 2013
SO201-2-85	57.505	170.413167	N. pachyderma	Reitdorf et al 2013
SO201-2-77	56.33	170.69883	N. pachyderma	Reitdorf et al 2013
SO201-2-12	53.992667	162.375833	N. pachyderma	Reitdorf et al 2013
MD01-2416	51.268	167.725	N. pachyderma	Gebhardt et al 2008
MD01-2416	51.268	167.725	G. bulloides	Gebhardt et al 2008
VINO-GGC37	50.28	167.7	N. pachyderma	Keigwin 1998
LV29-114-3	49.375667	152.877933	N. pachyderma	Reitdorf et al 2013
KT90-9_21	42.45	144.3167	G. bulloides	Oba and Murayama 2004
GH02-1030	42	144	G. bulloides	Sagawa and Ikehara 2008
CH84-14	41.44	142.33	G. bulloides	Labeyrie 1996
CH84-04	36.46	142.13	G. bulloides	Labeyrie 1996
MD01-2420	36.067	141.817	G. bulloides	Sagawa et al 2006
MD01-2421	36.01667	141.7833	G. bulloides	Oba and Murayama 2004
KY07_04_01	31.6391667	128.944	G. ruber	Kubota et al 2010
A7	27.82	126.98	G. ruber	Sun et al 2005
ODP184-1145	19.58	117.63	G. ruber	Oppo and Sun 2005

959

960

961

962

963

964

965

Table S2 Reconstructed change in gyre boundary latitude. Uncertainty is 1σ .

age	DLat	DLat_error	DLat_west	DLat_west_error	Dlat_east	DLat_east_error
10.5	0.0	1.0	0.0	1.3	0	1.0
11.0	-0.6	0.9	-0.7	1.2	-0.3	0.9
11.5	-1.0	0.9	-1.1	1.1	-0.5	1.0
12.0	-1.4	0.9	-1.7	1.1	-0.5	1.1
12.5	-1.5	0.9	-1.9	1.0	-0.8	1.1
13.0	-1.6	0.9	-1.8	1.0	-0.2	1.3
13.5	-1.6	0.9	-1.8	1.0	0	1.3
14.0	-1.5	0.9	-1.7	1.0	0.2	1.3
14.5	-1.5	0.9	-1.7	1.0	-0.5	1.2
15.0	-1.9	0.8	-1.9	1.0	-2.4	1.0
15.5	-2.3	0.8	-2.1	1.0	-3.9	1.0
16.0	-2.6	0.8	-2.1	1.0	-5	0.9
16.5	-2.8	0.9	-2.0	1.0	-5.9	0.9
17.0	-3.1	0.9	-2.0	1.0	-6.3	0.9
17.5	-3.2	0.9	-2.0	1.0	-6.3	1.0
18.0	-3.1	0.9	-2.0	1.0	-6.4	1.1
18.5	-3.1	0.9	NA	NA	-6	1.1

966

967 **Additional References**

- 968 Boyer, T.P., Antonov, J.I., Baranova, O.K., Coleman, C., Garcia, H.E., Grodsky, A., John-
969 R.A., Mishonov, A.V., O'Brien, T.D., Paver, C.R., Reagan, J.R., Seidov, D., Smolyar, I.V., Zweng, M.M., 2013.
970 World Ocean Database 2013. In: Levitus, Sydney (Ed.), Alexey Mishonov (Technical Ed.), NOAA Atlas
971 NESDIS, vol. 72. 209 pp.
- 972 Evans D., Wade B. S., Henehan M., Erez J. and Müller W. (2016) Revisiting carbonate chemistry controls on
973 planktic foraminifera Mg / Ca: Implications for sea surface temperature and hydrology shifts over the Paleocene-
974 Eocene Thermal Maximum and Eocene-Oligocene transition. *Clim. Past* 12.
- 975 Gebhardt, H. et al., Paleonutrient and productivity records from the subarctic North Pacific for Pleistocene glacial
976 terminations I to V. *Paleoceanography* 23, PA4212 (2008).
- 977 Gray, W. R., Weldeab, S., Lea, D. W., Rosenthal, Y., Gruber, N., Donner, B. and Fischer, G. (2018b) The effects of
978 temperature, salinity, and the carbonate system on Mg/Ca in *Globigerinoides ruber* (white): A global sediment
979 trap calibration. *Earth Planet. Sci. Lett.* 482, 607–620.
- 980 Gray, W.R. and Evans, D. (2019) Nonthermal influences on Mg/Ca in planktonic foraminifera: A review of culture
981 studies and application to the last glacial maximum. *Paleoceanography and Paleoclimatology*, 34. [https://doi.org/](https://doi.org/10.1029/2018PA003517)
982 [10.1029/2018PA003517](https://doi.org/10.1029/2018PA003517)
- 983 Harada, N. Ahagon, N., Uchida, M. (2004) Northward and southward migrations of frontal zones during the past 40
984 kyr in the Kuroshio-Oyashio transition area. *Geochemistry*, doi:10.1029/2004GC000740/pdf.
- 985 Harada, N. (2006) Rapid fluctuation of alkenone temperature in the southwestern Okhotsk Sea during the past 120
986 ky. *Global and Planetary Change.* 53, 29–46.
- 987 Harada, N., Sato, M., Sakamoto, T. (2008) Freshwater impacts recorded in tetraunsaturated alkenones and alkenone
988 sea surface temperatures from the Okhotsk Sea across millennial-scale cycles. *Paleoceanography.* 23, PA3201.
- 989 Harada, N., Sato, M., Sakamoto, T. (2008) Freshwater impacts recorded in tetraunsaturated alkenones and alkenone
990 sea surface temperatures from the Okhotsk Sea across millennial-scale cycles. *Paleoceanography.* 23, PA3201.
- 991 Hendy, I. L., Kennett, J. P., Roark, E. B., Ingram, B. L., (2002) Apparent synchronicity of submillennial scale climate
992 events between Greenland and Santa Barbara Basin, California from 30-10 ka. *Quaternary Science Reviews* 21,
993 1167-1184.
- 994 Herbert, D. et al. (2001) Collapse of the California Current During Glacial Maxima Linked to Climate Change on
995 Land. *Science.* 293, 71–76.

996 Hill, T.M., J.P. Kennett, D.K. Pak, R.J. Behl, C. Robert, and L. Beaufort. 2006. Pre-Bolling warming in Santa
997 Barbara Basin, California: surface and intermediate water records of early deglacial warmth. *Quaternary Science*
998 *Reviews* 25, pp. 2835–2845, doi:10.1016/j.quascirev.2006.03.012

999 Hönisch B., Allen K. a., Lea D. W., Spero H. J., Eggins S. M., Arbuszewski J., deMenocal P., Rosenthal Y., Russell
1000 A. D. and Elderfield H. (2013) The influence of salinity on Mg/Ca in planktic foraminifers – Evidence from
1001 cultures, core-top sediments and complementary $\delta^{18}\text{O}$. *Geochim. Cosmochim. Acta* 121, 196–213.

1002 Inagaki, M., Yamamoto, M., Igarashi, Y., Ikehara, K. (2009) Biomarker records from core GH02-1030 off Tokachi
1003 in the northwestern Pacific over the last 23,000 years: Environmental changes during the last deglaciation.
1004 *Journal of Oceanography*. 65, 847–858.

1005 Isono, D. et al. (2009) The 1500-year climate oscillation in the midlatitude North Pacific during the Holocene.
1006 *Geology*. 37, 591–594.

1007 Kisakürek, B., Eisenhauer, A., Böhm, F., Garbe-Schönberg, D., Erez, J., 2008. Controls on shell Mg/Ca and Sr/Ca
1008 in cultured planktonic foraminiferan, *Globigerinoides ruber* (white). *Earth Planet. Sci. Lett.* 273, 260–269.
1009 <https://doi.org/10.1016/j.epsl.2008.06.026>.

1010 Kubota, Y., K. Kimoto, R. Tada, H. Oda, Y. Yokoyama, and H. Matsuzaki (2010), Variations of East Asian summer
1011 monsoon since the last deglaciation based on Mg/Ca and oxygen isotope of planktic foraminifera in the northern
1012 East China Sea, *Paleoceanography*, 25, PA4205, doi:10.1029/2009PA001891.

1013 Labeurie, L. 1996. Quaternary paleoceanography: unpublished stable isotope records. IGBP PAGES/World Data
1014 Center for Paleoclimatology Data Contribution Series #1996-036. NOAA/NGDC Paleoclimatology Program,
1015 Boulder, Colorado, USA.

1016 Lea D. W., Mashiotta T. A. and Spero H. J. (1999) Controls on magnesium and strontium uptake in planktonic
1017 foraminifera determined by live culturing. *Geochim. Cosmochim. Acta* 63, 2369–2379.

1018 Maeda, L., H. Kawahata and M. Noharta (2002): Fluctuation of biogenic and abiogenic sedimentation on the Shatsky
1019 Rise in the western north Pacific during the late Quaternary. *Marine Geology* 189, 197-214.

1020 Minoshima, K., H. Kawahata, K. Ikehara (2007) Changes in biological production in the mixed water region (MWR)
1021 of the northwestern North Pacific during the last 27 kyr. *Palaeogeography, Palaeoclimatology, Palaeoecology*.
1022 254, 430–447.

1023 Mortyn, P. G., Thunell, R. C., Anderson, D. M., Stott, L. D., Le, J. (1996) Sea surface temperature changes in the
1024 Southern California Borderlands during the last glacial-interglacial cycle. *Paleoceanography* 11, 415-430.

1025 Narita, H., M. Sato, S. Tsunogai, M. Maruyama, M. Ikehara, T. Nkatsuka, M. Wakatsuchi, N. Harada and U. Ujiie
1026 (2002): Biogenic opal indicating less productive northwestern North Pacific during glacial stages. *Geophys. Res.*
1027 *Lett.*, 29(15), 22-1 to 22-4.

1028 Oba, T., Murayama, M. (2004) Sea-surface temperature and salinity changes in the northwest Pacific since the Last
1029 Glacial Maximum. *Journal of Quaternary Science* 19, 335-346.

1030 Oppo, D. W., and Y. Sun (2005) Amplitude and timing of sea surface temperature change in the northern South
1031 China Sea: Dynamic link to the East Asian monsoon. *Geology* 33, 785–788.

1032 Pak, D. K., D. W. Lea, and J. P. Kennett (2012) Millennial scale changes in sea surface temperature and ocean
1033 circulation in the northeast Pacific, 10–60 kyr BP, *Paleoceanography* 27, PA1212, doi:10.1029/2011PA002238.

1034 Peltier, W. R. (2004). Global glacial isostasy and the surface of the Ice-Age Earth: The ICE-5G (VM2) model and
1035 GRACE. *Annual Review of Earth and Planetary Sciences*, 32(1), 111–149.
1036 <https://doi.org/10.1146/annurev.earth.32.082503.144359>

1037 Praetorius, S. K., Mix, A. C. (2014) Synchronization of North Pacific and Greenland climates preceded abrupt
1038 deglacial warming. *Science* 345, 444. DOI: 10.1126/science.1252000.

1039 Prahl, F. G., L. A. Muehlhausen, and D. L. Zahnle (1988), Further evaluation of long-chain alkenones as indicators
1040 of paleoceanographic conditions, *Geochim. Cosmochim. Acta* 52, 2303–2310.

1041 Reimer, P. J. et al. (2013) IntCal13 and Marine13 radiocarbon age calibration curves 0-50,000 years cal BP.
1042 *Radiocarbon* 55, 1869–1887.

1043 Reiss, P. T., Ogden, R. T. (2009) Smoothing parameter selection for a class of semiparametric linear models. *Journal*
1044 *of the Royal Statistical Society B* 71, 505-523.

1045 Riethdorf, J.-R., Max, L., Nürnberg, D., Lembke-Jene, L., Tiedemann, R. (2013) Deglacial development of (sub)
1046 sea surface temperature and salinity in the subarctic northwest Pacific: Implications for upper-ocean
1047 stratification. *Paleoceanography*. 28, 91–104.

1048 Rodríguez Sanz, L., Mortyn, P. G., Herguera, J. C., Zahn, R. (2013) Hydrographic changes in the tropical and
1049 extratropical Pacific during the last deglaciation. *Paleoceanography*. 28, 529–538.

1050 Russell A. D., Hönisch B., Spero H. J. and Lea D. W. (2004) Effects of seawater carbonate ion concentration and
1051 temperature on shell U, Mg, and Sr in cultured planktonic foraminifera. *Geochim. Cosmochim. Acta* 68, 4347–
1052 4361.

1053 Sagawa, T., Toyoda, K., Oba, T. (2006) Sea surface temperature record off central Japan since the Last Glacial
1054 Maximum using planktonic foraminiferal Mg/Ca thermometry.
1055 Sagawa, T., Ikehara, K. (2008) Intermediate water ventilation change in the subarctic northwest Pacific during the
1056 last deglaciation. *Geophysical Research Letters* 35, L24702, doi:10.1029/2008GL035133.
1057 Seki, O., et al. (2004) Reconstruction of paleoproductivity in the Sea of Okhotsk over the last 30 kyr.
1058 *Paleoceanography*. 19, PA1016.
1059 Singarayer, J.S., Valdes, P.J., Friedlingstein, P., Nelson, S., Beerling, D.J., 2011. Late Holocene methane rise caused
1060 by orbitally controlled increase in tropical sources. *Nature* 470, 8285. <https://doi.org/10.1038/nature09739>
1061 Taylor, B.J., Rae, J.W.B., Gray, W.R., Darling, K.F., Burke, A., Gersonde, R., Abelman, A., Maier, E., Esper, O.,
1062 Ziveri, P. (2018) Distribution and ecology of planktic foraminifera in the North Pacific: Implications for paleo-
1063 reconstructions. *Quaternary Science Reviews* 191, 256-274.
1064 Taylor, M. A., Hendy, I. L., Pak, D. K. (2014) Deglacial ocean warming and marine margin retreat of the Cordilleran
1065 Ice Sheet in the North Pacific Ocean. *Earth and Planetary Science Letters*. 403, 89–98 (2014).
1066 Tierney J. E. and Tingley M. P. (2018) BAYSPLINE: A New Calibration for the Alkenone Paleothermometer.
1067 *Paleoceanogr. Paleoclimatology* 33, 281–301.
1068 Yamamoto, M., Oba, T., Shimamune, J., Ueshima, T. (2004) Orbital-scale anti-phase variation of sea surface
1069 temperature in mid-latitude North Pacific margins during the last 145,000 years. *Geophysical Research Letters*.
1070 31, L16311.
1071 Zahn, R., Pedersen, T. F., Bornhold, B. D., Mix, A. C. (1991) Watermass conversion in the glacial subarctic Pacific
1072 (54°N, 148°W): physical constraints and the benthic-planktonic stable isotope record. *Paleoceanography* 6, 543-
1073 560.
1074